

Research paper

Computational analysis of an ammonia-fuelled hybrid solid oxide fuel cell–gas turbine propulsion system for commercial aviation

Luca Wagner, Efstathios-Al. Tingas¹*

School of Computing, Engineering and the Built Environment, Edinburgh Napier University, Edinburgh, EH10 5DT, UK



ARTICLE INFO

Keywords:

Hydrogen
Ammonia
Solid oxide fuel cell
Hybrid
Gas turbine
Turbofan

ABSTRACT

This study investigates the performance of a hybrid solid oxide fuel cell–gas turbine (SOFC-GT) propulsion system for commercial aviation, using ammonia–hydrogen blends as fuel. A computational model was developed by combining NASA's T-MATS toolbox with Cantera-based chemical equilibrium calculations to simulate thermodynamic, aerodynamic, and electrochemical interactions. The analysis examined key design and operational parameters, including fan pressure ratio (FPR), bypass ratio (BPR), equivalence ratio, altitude, and Mach number. Results showed that pure ammonia produced the highest thrust (14.5 MW total power and 2.2 kg/s fuel flow) but at the cost of lower thermal efficiency and higher specific fuel consumption (SFC). Increasing the hydrogen content in the fuel reduced fuel flow by up to 86%, improved thermal efficiency by 4.5%, and eliminated CO₂ emissions, though NO emissions increased by 20%. Variations in equivalence ratio demonstrated a trade-off between thrust and efficiency, with net thrust increasing by 68% and thermal efficiency decreasing by 34% as equivalence ratio rose from 0.24 to 0.8. Optimal FPR and BPR combinations improved net thrust by up to 35% and reduced SFC by 26%. Although the hybrid system's power-to-weight ratio was 30%–37% lower than that of a conventional turbofan, advancements in lightweight SOFC materials and designs could enhance feasibility. These findings demonstrate the potential of SOFC-GT systems to enable zero-carbon aviation while maintaining competitive performance metrics.

1. Introduction

The aviation sector, responsible for 2.1% of global anthropogenic emissions must address stricter environmental regulations [1] and industry commitments [2] as air traffic is projected to grow by 3.1% annually until 2050 [3]. Electrified systems have emerged as a pathway to greater efficiency and lower emissions, with fuel cells being the only energy source capable of meeting the high energy density and endurance requirements of large, long-range passenger aircraft [4]. Among fuel cell technologies, proton exchange membrane fuel cells (PEMFCs) and solid oxide fuel cells (SOFCs), are prominent. While PEMFCs are commercially advanced, they face challenges such as narrow operating temperature ranges, complex water management, and limited fuel flexibility. SOFCs, by contrast, offer high efficiency (60%–65%), fuel versatility, and effective heat recovery, making them well-suited for large-scale aviation applications [5].

SOFC-gas turbine (SOFC-GT) hybrid propulsion systems combine the efficiency and fuel flexibility of SOFCs with the power density and operational versatility of gas turbines. These systems achieve significant reductions in greenhouse gas and nitrogen oxide emissions [6] while supporting alternative fuels, including hydrogen, making them

a cornerstone for sustainable aviation. Beyond aviation, SOFC-GT systems also show promise in stationary power generation, contributing to decarbonisation across multiple sectors.

The integration of SOFCs with gas turbines has been extensively studied for power generation, leveraging the thermal synergy between the systems to achieve high efficiencies [7]. Building on this success, research has shifted towards aviation propulsion, exploring hybrid SOFC-GT systems and turbine-less jet engines where SOFCs replace turbines to power compressors. Ji et al. [8] demonstrated that these configurations eliminate turbine-related temperature constraints, enabling higher combustion temperatures and significant improvements. For instance, integrating steam injection and SOFCs into turbine-less engines fuelled by propane or methane resulted in specific impulse and thrust increases of up to 51%, with thermal efficiencies reaching 57.6% under design conditions [9]. Operational studies identified optimal zones free from turbine inlet temperature limitations, ensuring reliability and efficiency [10]. Additionally, strategies such as regulating fuel flow in the afterburner and optimising fuel cell size and equivalence ratios further enhanced endurance, achieving up to a 15.2% improvement compared to traditional turbojet engines [11].

* Corresponding author.

E-mail address: e.tingas@napier.ac.uk (E.-A. Tingas).

Nomenclature

A	Area [m ²]
A_{cell}	Active cell area [m ²]
a	Speed of sound [m s ⁻¹]
AFR	Air-fuel ratio
BPR	Bypass ratio
C	Heat capacity [W K ⁻¹]
c_p	Specific heat capacity [J kg ⁻¹ K ⁻¹]
C_r	Thermal capacity ratio
D_{eff}	Average effective mass diffusivity coefficient [m s ⁻²]
E_{act}	Activation energy [J mol ⁻¹]
F	Faraday's constant [C mol ⁻¹]
f	Fuel-to-air ratio
FPR	Fan pressure ratio
G	Gibbs free energy [J]
GT	Gas Turbine
h	Enthalpy [J kg ⁻¹]
j	Current density [A m ⁻²]
$j_{0,anode}$	Exchange current density at the anode [A m ⁻²]
$j_{0,cathode}$	Exchange current density at the cathode [A m ⁻²]
K_{eq}	Equilibrium constant
\dot{m}	Mass flow rate [kg s ⁻¹]
LHV	Lower Heating Value
M_∞	Freestream Mach number
N_{cell}	Number of cells in the SOFC stack
N_{stacks}	Number of stacks in the SOFC stack
NTU	Number of transfer units
n_e	Number of electrons involved in the reaction
n_i	Number of moles of species
P	Pressure [Pa]
p	Partial pressure [Pa]
PtW	Power-to-Weight
Q	Heat added to the system [J]
\dot{Q}	Heat transfer rate [W]
\dot{Q}_{Decomp}	Added heat through decomposition (W)
\dot{Q}_{SOFC}	Heat input to the SOFC [W]
R	Universal gas constant [J mol ⁻¹ K ⁻¹]
R_{ohm}	Fuel cell internal resistance [Ω m ²]
S	Entropy [J K ⁻¹]
SFC	Specific fuel consumption [kg/s/kN]
$SOFC$	Solid Oxide Fuel Cell
T	Temperature [K]
U	Internal energy [J]
u	Flight Speed [m s ⁻¹]
u_{ec}	Exhaust Velocity of Bypass Air [m s ⁻¹]
u_{eh}	Exhaust Velocity of Hot Gases [m s ⁻¹]
u_f	Fuel utilisation
U_{htc}	Overall heat transfer coefficient [W m ⁻² K ⁻¹]
V	Actual electromotive force [V]
v_e	Nozzle exit velocity [m s ⁻¹]
V_r	Nernst electromotive force [V]

V_r°	Standard Nernst electromotive force [V]
W	Work done by the system [J]
W_{SOFC}	Power output from the SOFC [W]
z	Number of moles of electrons transferred
η_{conc}	Concentration polarisation loss [V]
η_{max}	Maximum electrical efficiency
η_{act}	Activation polarisation loss [V]
η_{ohm}	Ohmic polarisation loss [V]
$\eta_{SOFC,th}$	Thermal efficiency of the SOFC
μ_i	Chemical potential of species i

Subscripts

a	Air
b	Burner
c	Cold fluid
c	Compressor
cb	Cold bypass air
d	Duct
eh	Hot exhaust gases
f	Fuel
fa	Fan
g	Gross
h	Hot fluid
HPC	High pressure compressor
HPT	High pressure turbine
H ₂	Hydrogen
H ₂ O	Water vapour
in	Inlet
LPC	Low pressure compressor
LPT	low pressure turbine
max	Maximum
min	Minimum
n	Nozzle
net	Net
N ₂	Nitrogen
NH ₃	Ammonia
o	Overall
out	Outlet
O ₂	Oxygen
p	Propulsive
ram	Ram
t	Turbine
th	Thermal
TPB	Three phase boundary

Greek symbols

α	Transfer coefficient
η	Efficiency
Γ	Thrust (N)
γ	Ratio of specific heats
κ	Pre-exponential coefficient (A m ⁻²)
δ	Infinitesimal change
π	Pressure ratio
σ	Electronic conductivity (Ω^{-1} m ⁻¹)
τ	Thickness (m)
ε	Effectiveness of the heat exchanger
ξ	Pressure recovery coefficient

The choice of fuel plays a critical role in the performance and feasibility of hybrid SOFC-GT propulsion systems. Inarguably, most existing works have utilised carbon-based fuels: natural gas or methane [12], propane [13], methane/propane blends [8], methane/hydrogen blends [14], methanol [15], methanol/hydrogen blends [16], ethanol [17], ethanol/hydrogen blends [16], DME [18], DME/hydrogen [16], methanol/ethanol/methane/DME/hydrogen blends [16], tetra/n-decane [19], n-octane [17], kerosene [20], JP4 [21], JP5 [21], JP10 [21]. Some considerable body of literature also has been dedicated to hydrogen [22]. Notably, only one study has investigated the use of ammonia in a turbine-less SOFC configuration [23]. Ammonia offers several advantages over hydrogen, particularly regarding storage convenience and higher volumetric energy density [24]. Unlike hydrogen, which requires cryogenic temperatures or high pressures for storage, ammonia can be stored as a liquid under moderate conditions, making it more practical and cost-effective for large-scale use in aviation [23]. Studies have demonstrated the feasibility of ammonia combustion in gas turbines, with necessary modifications to accommodate its combustion properties, thereby highlighting the potential for ammonia-powered aviation applications [25]. Additionally, ammonia is already widely produced and transported globally as a commodity chemical, primarily for fertilisers, making its adoption logistically feasible. The maritime industry is considering ammonia as a means to achieve decarbonisation due to its carbon-free nature when used as a fuel, which could facilitate the development of infrastructure beneficial to aviation [23]. Ships can utilise onboard ammonia cracking to produce hydrogen for fuel cells or combustion engines, addressing storage and infrastructure challenges associated with hydrogen fuel [26].

However, ammonia presents challenges that need to be addressed [27]. Its toxicity poses safety risks in handling and potential environmental hazards in case of leaks or spills [28]. Moreover, ammonia has a low flame speed and poor combustion reactivity, making it less suitable for direct use in gas turbines and internal combustion engines [29]. These properties can lead to incomplete combustion, lower efficiency, and higher emissions of unburned ammonia and nitrogen oxides (NOx) [30]. To overcome the low reactivity of ammonia, an effective strategy is to enrich it with hydrogen [30]. Ammonia can act as a hydrogen carrier; by cracking a portion of the stored ammonia onboard the aircraft, hydrogen is produced and then mixed with the remaining ammonia [29]. This hydrogen-enriched ammonia fuel enhances the combustion process by increasing flame speed and stability, leading to more efficient and complete combustion [31]. This approach not only improves engine performance but also addresses emissions issues associated with pure ammonia combustion.

Given these considerations, the current work is a computational study of a hybrid system integrating a SOFC with a commercial turbofan engine, using ammonia as the main fuel. By leveraging the benefits of ammonia and addressing its challenges through hydrogen enrichment, this study seeks to explore the viability of ammonia-fuelled SOFC-gas turbine hybrid systems for aero-propulsion, contributing to the development of sustainable and efficient aviation technologies. The objectives of the current can be summarised as follows: (i) to assess the performance of the hybrid system against that of a pure turbofan engine; (ii) evaluate the performance (including emissions) of the hybrid system under varying operational conditions; (iii) to quantify the effect of key design parameters, namely the fan pressure ratio and bypass ratio on the system's performance. To achieve these objectives, a new computational model is developed, based on NASA's Toolbox for the Modelling and Analysis of Thermodynamic Systems (T-MATS).

The structure of the paper is as follows. Firstly, the overall model is described. Starting from the T-MATS brief description, detailed descriptions of the models used for the reformer, the SOFC and the heat exchanger follow. Both the SOFC and the GT models are validated against experimental data reported in the literature. The analysis

follows, which is divided into four subsections: (i) the comparison between the pure turbofan engine and the hybrid SOFC-GT system; (ii) the effect of flight altitude and mach number on engine performance; (iii) the effect of equivalence ratio on engine performance; (iv) the effect of fan pressure ratio and bypass ratio on engine performance.

2. Materials and methods

This section outlines the modelling framework developed to simulate the hybrid SOFC-GT propulsion system. It begins with a description of the overall system configuration and follows with detailed accounts of the individual components—namely, the turbofan engine, decomposition reactor, SOFC, and heat exchangers. The modelling approach integrates thermodynamic, electrochemical, and fluid dynamic principles using NASA's T-MATS and Cantera. Validation steps and key assumptions are also presented to establish the reliability of the simulation results.

2.1. Overall system description

The hybrid propulsion system, as illustrated in Fig. 1, integrates a two-spool, high-bypass turbofan engine — specifically the JT9D model manufactured by Pratt & Whitney (see the Supplementary material for the engine's specifications)—with a SOFC. A detailed flowchart illustrating the integration and data flow between system components is provided in the supplementary material, along with the definition of the key metrics used to evaluate the system's performance. Ambient air enters the engine through the inlet and is accelerated by the fan, after which the airflow is divided into two streams. One stream, called bypass air, flows around the engine core, while the other, core air, passes through the low- and high-pressure compressors to undergo further compression, increasing its pressure and temperature. After high-pressure compression, the core airflow is split once again. A portion of the air, determined by the engine's bypass ratio, is directed to a counterflow heat exchanger, where it is preheated before entering the SOFC. The remaining air bypasses this heat exchanger and flows directly to the combustion chamber. In the heat exchanger, the preheated air reaches the operational temperature necessary for the SOFC and is routed to the cathode side of the fuel cell, with the heat energy supplied by the turbine exhaust gases. Simultaneously, fuel (ammonia) from onboard tanks is routed through a second counterflow heat exchanger, where it is preheated before being fed into the external decomposition reactor. In this reactor, the fuel undergoes partial cracking, producing two distinct flows of hydrogen: one directed to the anode of the SOFC, and the other routed directly to the combustion chamber where hydrogen mixes with ammonia. The ratio of hydrogen fuel distributed between the SOFC and combustion chamber can be adjusted according to the combustion chamber's operational requirements at any given time. Also, the ratio of ammonia/hydrogen in the fuel blend that is used in the combustor can vary but in principle, the thinking is to maintain the hydrogen content there as low as operationally possible. It is also noted that a small hydrogen quantity that slips the SOFC is also fed into the combustor. The motivation of adding hydrogen in the ammonia fuelled combustor is to enhance the system's operational flexibility as ammonia/air flames are notoriously difficult to stabilise in a wide range of operational conditions due to ammonia's poor reactivity and flame speed; adding hydrogen (which is significantly more reactive) in such flames is a well documented method of addressing the combustion challenges posed by ammonia [32]. The SOFC operates by receiving preheated air from the heat exchanger and fuel from the decomposition reactor, generating exhaust gases. These exhaust gases, along with the fuel mixture from the reactor and bypass air, are introduced into the combustion chamber, where they ignite to produce high-energy gases. These gases expand through the turbine, driving the fan and compressors. Finally, the residual gases are expelled through the exhaust nozzle, contributing to the overall thrust generation.

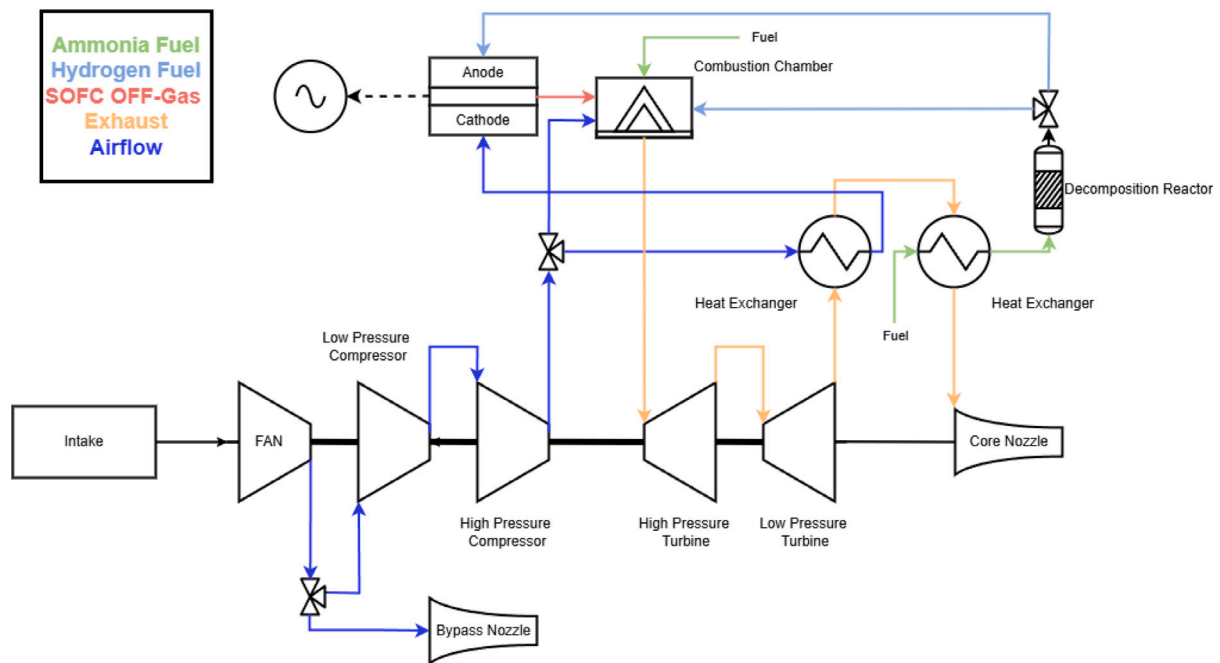


Fig. 1. The layout of the hybrid SOFC-GT system employed in the current study.

2.2. System modelling

The subsequent section provides a detailed description of the system modelling for the SOFC-GT hybrid system. This includes the modelling of the turbofan engine, the SOFC, the heat exchanger and the decomposition reactor, all of which are essential components for conducting the thermodynamic performance analysis. Both the decomposition reactor and heat exchanger sub-models were developed in MATLAB using Level-2 S-Functions and integrated into the Simulink environment, consistent with the T-MATS framework used for the rest of the system components.

2.2.1. Turbofan engine modelling

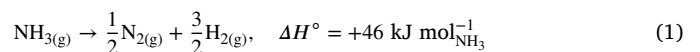
For the development of the current study's hybrid system model, T-MATS was employed [33], which is a versatile, open-source simulation toolbox developed to facilitate the dynamic modelling, simulation, and analysis of thermodynamic systems [34]. It is implemented in MATLAB/Simulink, providing a user-friendly interface to model complex systems, particularly those involving gas turbine engines and other aerospace propulsion systems [35]. T-MATS is specifically designed to handle systems involving fluids, heat transfer, and mechanical power generation by offering a comprehensive suite of tools for simulating components such as compressors, turbines, heat exchangers, and fuel cells [36]. The toolbox integrates component-level models with thermodynamic principles, allowing users to simulate how energy, mass, and heat interact in real-time under various operating conditions. In addition, the toolbox enabled the modelling of key components, including the high-bypass turbofan engine and the SOFC, and their interactions within the propulsion cycle. By using T-MATS, the system's steady-state behaviour could be analysed, with its extensive libraries of thermodynamic models ensuring accurate prediction of system performance under varying loads and environmental conditions. Moreover, T-MATS's flexibility allowed for the incorporation of custom sub-models for fuel decomposition and heat exchangers, which are integral to this hybrid propulsion configuration. To further enhance the modelling capabilities, the implementation of Cantera was employed [37]. Cantera enables the inclusion of complex chemical kinetics, thereby allowing for the simulation of more sophisticated systems. This simulation approach provided the foundation for detailed

performance evaluation and optimisation of the system. For a more detailed description of the turbofan model the reader is referred to the Supplementary material.

To assess the turbofan model's accuracy, its performance was validated using literature data [37]. This process involved a detailed comparison between the model's simulation outputs and the literature results, as illustrated in Table 1. The simulations were conducted under conditions typical for turbofan operations, with a Mach number of 0.8 and an altitude of 34,000 ft (10,36 km). The comparison showed that the simulation results exhibited an absolute error of approximately $\pm 4.8\%$, aligning closely with the experimental data. Given the small error observed, it can be inferred that the turbofan model accurately captures the primary thermodynamic processes within the specified range of operation.

2.2.2. Decomposition reactor modelling

In the employed model, the main fuel, i.e., ammonia, is decomposed into hydrogen and nitrogen, through an external reformer. Part of the produced hydrogen is fed into the SOFC for the normal operation of the SOFC while the remaining hydrogen is fed into the combustor of the JT9D engine, to enhance the performance of the combustor. The decomposition of ammonia for use in fuel cells is a critical process, which in the current work it is modelled according to the following reaction:



Here, ΔH denotes the reaction enthalpy change, indicating an endothermic reaction. The position of thermodynamic equilibrium for the reaction is determined by minimising the system's total Gibbs free energy. This principle of thermodynamics implies that the equilibrium state corresponds to the lowest possible Gibbs energy under the given conditions of temperature and pressure:

$$\Delta G_{ADR,T,p} = 0 \quad (2)$$

where $\Delta G_{ADR,T,p}$ represents the Gibbs energy of the ammonia decomposition reaction at a specific temperature (T) and pressure (p). Subsequently, the equilibrium composition of the ideal gas mixture is

Table 1
JT9D turbofan validation at Mach 0.8 and at 34,000 ft (10.36 km). For the validation, the literature data reported in [37] was used.

Conditions	Literature data Mach number (0.8)	Experimental data Altitude (34,000 ft)
Weight flow	674 lbm/s (305.78 kg/s)	674.2 lbm/s (305.87 kg/s)
Thrust	11,182 lbf (49.7 kN)	11,750 lbf (52.3 kN)
Specific fuel consumption	0.6116 (lbm/h)/lbf [0.0174 (kg/s)/kN]	0.5922 (lbm/h)/lbf [0.0168 (kg/s)/kN]

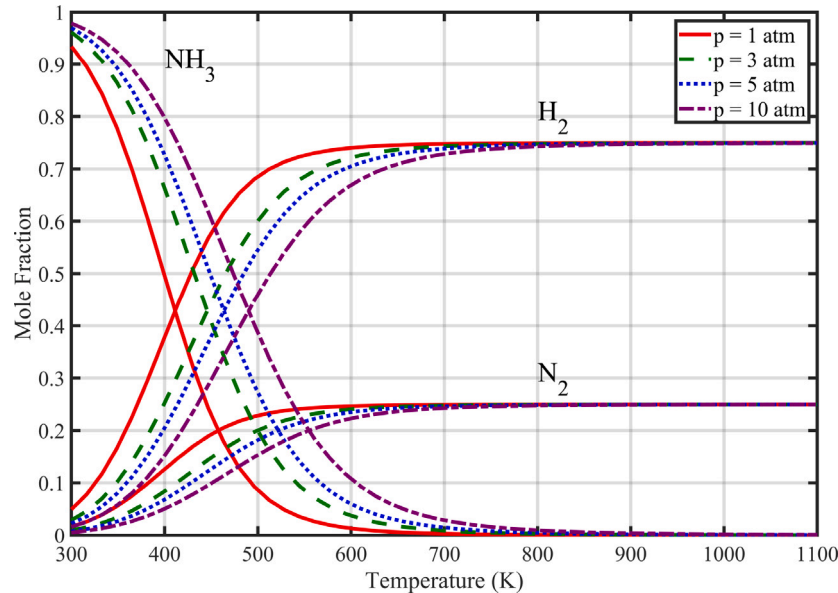


Fig. 2. Ammonia decomposition at different pressures and temperatures.

characterised using the chemical equilibrium constant, as described by the following expression:

$$K_{eq} = e^{-\frac{\Delta G(T,p)}{RT}} \quad (3)$$

where K_{eq} is the equilibrium constant, $\Delta G(T,p)$ is the Gibbs energy change, and R is the universal gas constant. However, the equilibrium constant can also be expressed in terms of the partial pressures:

$$K_{eq} = \frac{p_{N_2}^{1/2} p_{H_2}^{3/2}}{p_{NH_3}} \quad (4)$$

where p_{N_2} , p_{H_2} and p_{NH_3} the partial pressures of nitrogen, hydrogen and ammonia, respectively.

The first law of thermodynamics can be applied to derive the mass and enthalpy relation in a reactor where the ammonia decomposition reaction takes place. The law is expressed as:

$$\Delta U = Q - W \quad (5)$$

where ΔU is the change in internal energy, Q is the heat added to the system and W is the work done by the system. The equation can be expressed to the mass and enthalpy relation used in this context:

$$m_{out}h_{out} = m_{in}h_{in} + Q \quad (6)$$

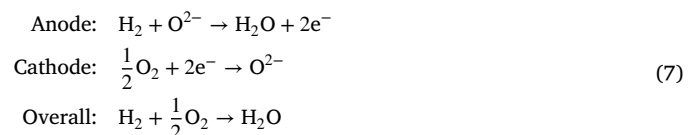
This equation correlates the mass flow rates (m_{in} , m_{out}) (kg s^{-1}) and specific enthalpies (h_{in} , h_{out}) (J kg^{-1}) at the inlet and outlet with Q , the net heat transfer to the system. It is noted that the decomposition of ammonia, described by Eq. (1), is an endothermic reaction.

Fig. 2 illustrates the relationship between temperature and pressure during the ammonia decomposition process. It can be observed that ammonia decomposition is favoured at high temperatures and low pressures, with complete decomposition achievable at 700 K and 1 atm. The decomposition model aligns with data reported in the literature [23,38].

In the employed model, the decomposition reactor is assumed to operate at a fixed outlet temperature, maintained by external heat input supplied via a counterflow heat exchanger. The reactor is thus modelled as isothermal, with no internal temperature variation. The energy required to sustain this temperature and drive the endothermic ammonia decomposition (Eq. (1)) is explicitly computed using the enthalpy balance (Eq. (6)), and is included in the system energy analysis (see Eq. 22, Table 3 in the Supplementary material). This approach ensures that while the reactor temperature is fixed, the associated thermal energy demand is dynamically captured and contributes to the overall energy balance of the hybrid system.

2.2.3. Solid oxide fuel cell modelling

In a SOFC, the electrochemical process initiates at the anode, where hydrogen undergoes oxidation, resulting in the formation of protons (H^+), electrons (e^-) and water (H_2O). The generated electrons flow through an external circuit, thereby producing an electric current as they move towards the cathode. Concurrently, oxygen molecules (O_2) at the cathode are reduced by gaining electrons to form oxygen ions (O^{2-}). These oxygen ions migrate through the dense, solid oxide electrolyte, typically made of yttria-stabilised zirconia (YSZ), towards the anode. At the anode, the oxygen ions react with the protons generated from the fuel oxidation, forming water and completing the electrochemical reaction. This process enables the SOFC to efficiently convert the chemical energy of the fuel directly into electrical energy, as shown in Eq. (7).



As the reforming of the fuel is carried out externally, the SOFC only utilises H_2 , therefore the electrochemical reaction can be modelled by

Eq. (7). The electrochemical behaviour of the SOFC is modelled starting from the Nernst electromotive force (V_r), given by Eq. (8)

$$V_r = V_r^\circ + \Delta V_r = \frac{-\Delta G}{zF} + \frac{RT}{2F} \ln \left(\frac{p_{H_2} \cdot p_{O_2}^{1/2}}{p_{H_2O}} \right) \quad (8)$$

where V_r° the standard Nernst electromotive force, ΔG is the Gibbs free energy change, z the number of electrons transferred per reaction, F the Faraday constant, R the universal gas constant and p_{H_2} , p_{H_2O} , $p_{O_2}^{1/2}$ the partial pressures related to H_2 , H_2O and O_2 , respectively. The actual cell voltage is calculated by accounting for ohmic, activation, and concentration losses as Eq. (9):

$$V = V_r - \eta_{ohm} - \eta_{act} - \eta_{conc} \quad (9)$$

where η_{ohm} the ohmic loss, η_{act} the activation polarisation loss and η_{conc} the concentration polarisation losses. The ohmic loss is estimated by Eq. (10):

$$\eta_{ohm} = j R_{ohm} = j \left(\frac{\tau_{anode}}{\sigma_{anode}} + \frac{\tau_{cathode}}{\sigma_{cathode}} + \frac{\tau_{electrolyte}}{\sigma_{electrolyte}} \right) \quad (10)$$

where j is the current density, R_{ohm} is the fuel cell internal resistance, τ is the thickness (of the anode, cathode and electrolyte), and σ the electronic conductivity. Activation polarisation losses at the electrodes are resolved using the Butler-Volmer formulation, as in Eqs. (11)–(13):

$$\eta_{act} = \eta_{act,anode} + \eta_{act,cathode} = \frac{RT}{2\alpha_{anode}F} \sinh^{-1} \left(\frac{j}{2j_{0,anode}} \right) + \frac{RT}{2\alpha_{cathode}F} \sinh^{-1} \left(\frac{j}{2j_{0,cathode}} \right) \quad (11)$$

$$j_{0,anode} = \kappa_{anode} \left(\frac{P_{H_2}}{P_{ref}} \right) \left(\frac{P_{H_2O}}{P_{ref}} \right) \exp \left(-\frac{E_{act,anode}}{RT} \right) \quad (12)$$

$$j_{0,cathode} = \kappa_{cathode} \left(\frac{P_{O_2}}{P_{ref}} \right)^{0.25} \exp \left(-\frac{E_{act,cathode}}{RT} \right) \quad (13)$$

where $j_{0,anode}$ and $j_{0,cathode}$ the exchange current density at the anode and cathode, respectively, α the transfer coefficient, κ the pre-exponential coefficient and the subscripts ref and TPB denote the reference atmospheric pressure and the three phase boundary, respectively. The concentration polarisation losses are given by Eq. (14):

$$\eta_{conc} = \eta_{conc,anode} + \eta_{conc,cathode} = \frac{RT}{2F} \ln \left(\frac{p_{H_2O,TPB} \cdot p_{H_2,f}}{p_{H_2O,f} \cdot p_{H_2,TPB}} \right) + \frac{RT}{4F} \ln \left(\frac{p_{O_2,anode}}{p_{O_2,TPB}} \right) \quad (14)$$

with partial pressures evaluated at the triple-phase boundary (TPB) and fuel inlet. The change in Gibbs free energy is computed via Eq. (15):

$$dG = V dP - S dT + \sum_i \mu_i dn_i \quad (15)$$

and related to enthalpy (H) and entropy (S) through Eq. (16):

$$\Delta G = \Delta H - T \Delta S. \quad (16)$$

The ideal efficiency of the fuel cell is given by Eq. (17):

$$\eta_{max} = \frac{\Delta G}{\Delta H} \cdot 100\% \quad (17)$$

while the practical electrical efficiency is given by Eq. (18):

$$\eta_{max} = \mu_f \frac{V}{1.25} \cdot 100\% \text{ (LHV)} \quad (18)$$

where μ_f is the fuel utilisation factor and V is the actual voltage. The thermal efficiency of the SOFC is defined as:

$$\eta_{SOFC,th} = \frac{\dot{W}_{SOFC}}{\dot{Q}_{SOFC}} \quad (19)$$

where \dot{W}_{SOFC} the power output from the SOFC and \dot{Q}_{SOFC} the heat input rate to the SOFC. The AC power output is computed from Eq. (20):

$$\dot{W}_{SOFC,AC} = j A_{cell} V N_{cell} \quad (20)$$

where A_{cell} the active cell area and N_{cell} the number of cells in the SOFC stack.

Table 2 presents the specifications of the SOFC utilised in the current study, outlining critical operational and design parameters essential for assessing its performance. The SOFC operates at a pressure of 100 kPa and a temperature of 975 K, with a current density of 500 mA/cm² and an exchange current density of 300 mA/cm², indicating its electrochemical activity. The anode, cathode, and electrolyte have thicknesses of 1.0×10^{-3} m, 2.0×10^{-5} m, and 8.0×10^{-6} m, respectively. The electronic conductivities of the anode and cathode are $80,000 \Omega^{-1} \text{ m}^{-1}$ and $8000 \Omega^{-1} \text{ m}^{-1}$, while the electrolyte conductivity follows a temperature-dependent relation, $33,400 \exp(-10,300/T) \Omega^{-1} \text{ m}^{-1}$, highlighting its impact on ionic conduction. The anode and cathode average effective mass diffusivity coefficients are $3.66 \times 10^{-5} \text{ m}^2 \text{ s}^{-1}$ and $1.37 \times 10^{-5} \text{ m}^2 \text{ s}^{-1}$, respectively, influencing species transport within the electrodes. Reaction kinetics parameters include pre-exponential coefficients of $7.0 \times 10^9 \text{ A m}^{-2}$ for the anode and $2.9 \times 10^9 \text{ A m}^{-2}$ for the cathode, as well as activation energies of $120,000 \text{ J mol}^{-1}$ for both electrodes. The electrolyte has a thickness of 1.0 mm and a resistivity of 0.3 ohm cm, which are vital for understanding ionic conductivity and overall efficiency. Furthermore, the active cell area is 0.09 m², consisting of 100 cells per stack and a total of 28 stacks, contributing to a hydrogen utilisation of 85%. These specifications provide a comprehensive framework for evaluating the SOFC's operational capabilities and efficiency in the context of the study.

The accuracy of the proposed SOFC model was validated using both simulation data from the literature [37] and experimental measurements reported in prior studies [41]. The validation process involved a comparative analysis between the simulated results and the empirical data, as depicted in Fig. 3. At the design point of 5000 mA/m² under operating conditions of 800 °C and 1 atm, the model predicted a voltage of 0.9568 V, closely aligning with the experimentally measured value of 0.94429 V. This corresponds to a relative error of 0.01324%, demonstrating a strong correlation with experimental observations. Additionally, an analysis over the entire current density range showed an average error of 0.9310% and a maximum error of 2.49%, further corroborating the model's accuracy. Given the low error margins, the proposed thermodynamic SOFC model satisfies the stringent accuracy requirements necessary for this analysis.

2.2.4. Heat exchanger modelling

In the current study, the heat exchanger recovers waste heat from the LPT to serve two functions: (i) preheat properly the incoming air and fuel before they enter the fuel cell; (ii) supply the necessary heat to the reformer to crack ammonia and produce hydrogen. The heat exchanger was modelled as an adiabatic component. To determine the outlet conditions for these flows, the effectiveness-Number of Transferred Units (NTU) method was utilised. This method is particularly advantageous when only the inlet conditions are known. In the design process, a counterflow arrangement was implemented to optimise thermal performance. The mathematical framework used to model the heat exchanger is provided in the Supplementary material.

3. Results and discussion

The analysis evaluates the performance of the hybrid SOFC-GT system compared to a conventional turbofan engine powered by Jet-A fuel. In addition, a series of parametric studies are conducted to explore key performance indicators and emissions characteristics under varying conditions. Both systems are assumed to operate under cruise

Table 2
SOFC specifications.

Parameter	SOFC	Units
Operating temperature, T	973 [17]	K
Current density, j	5000 [39]	$A\ m^{-2}$
Exchange current density, j_0	3000 [39]	$A\ m^{-2}$
Anode thicknesses, τ_{anode}	1.0×10^{-3} [39]	m
Cathode thicknesses, $\tau_{cathode}$	2.0×10^{-5} [39]	m
Electrolyte thicknesses, $\tau_{electrolyte}$	8.0×10^{-6} [39]	m
Anode electronic conductivity, σ_{anode}	80,000 [17]	$\Omega^{-1}\ m^{-1}$
Cathode electronic conductivity, $\sigma_{cathode}$	8000 [17]	$\Omega^{-1}\ m^{-1}$
Electrolyte electronic conductivity, $\sigma_{electrolyte}$	$33,400\exp(-10,300/T)$ [17]	$\Omega^{-1}\ m^{-1}$
Anode average effective mass diffusivity coefficient, $D_{eff,anode}$	3.66×10^{-5} [39]	$m\ s^{-2}$
Cathode average effective mass diffusivity coefficient, $D_{eff,cathode}$	1.37×10^{-5} [39]	$m\ s^{-2}$
Pre-exponential coefficient for anode, κ_{anode}	7.0×10^9 [18]	$A\ m^{-2}$
Pre-exponential coefficient for cathode, $\kappa_{cathode}$	2.9×10^9 [18]	$A\ m^{-2}$
Anode activation energy, $E_{act,anode}$	120,000 [18]	$J\ mol^{-1}$
Cathode activation energy, $E_{act,cathode}$	120,000 [18]	$J\ mol^{-1}$
Active cell area, A_{cell}	0.09 [18]	m^2
N_{cell} in one stack	100 [14,18]	-
N_{stacks}	28 [14]	-
Number of electrons transferred per reaction, z	2 [37]	-
Fuel utilisation, μ_f	85 [40]	%

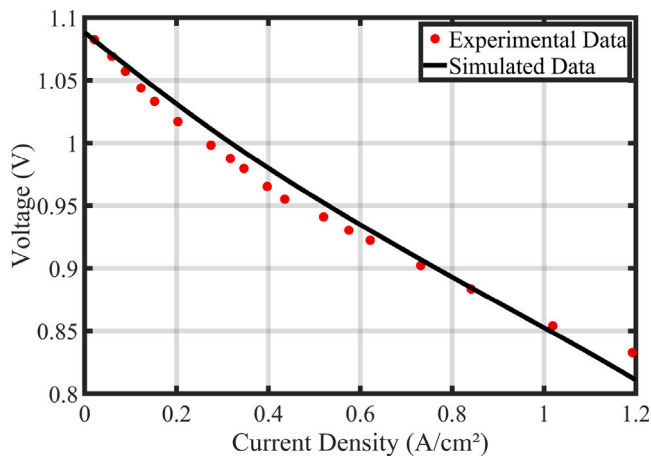


Fig. 3. SOFC Validation at 800 °C and 1 atm. For the validation, the experimental data reported in [41] was used.

conditions at an altitude of 34,000 ft (10.36 km) and a Mach number of 0.8. The corresponding airspeed is 238.7 m/s, with an air mass flow rate of 305.18 kg/s. As the JT9D is a two-spool engine, its design includes two turbines driving two compressors and the fan. The turbines are sized to provide adequate power to the compressors and fan, while any excess power is utilised to support onboard systems and, in the case of the hybrid SOFC-GT system, to complement the SOFC. The performance parameters of the SOFC, detailed in Table 3, include a net power output of 985 kW, an operating voltage of 0.8052 V, and an electrical efficiency of 54.75%, paired with a thermal efficiency of 65.50%. The specific power density is measured at 0.4026 W/cm², with a hydrogen mass flow rate of 12.77 g/s. Unless otherwise specified, the hybrid SOFC-GT system utilises a fuel mixture consisting of 10% hydrogen and 90% ammonia on a molar basis, with the feasibility of these conditions demonstrated under experimental settings [42].

The analysis is organised into four primary sections, each addressing critical aspects of system performance to ensure a comprehensive understanding of the hybrid SOFC-GT system's capabilities and limitations. The Section 1 compares the performance of the hybrid SOFC-GT system fuelled by various ammonia/hydrogen blends (ranging from 0% to 100% hydrogen) against the conventional JT9D engine fuelled by Jet-A. This section is motivated by the need to evaluate the viability of ammonia-hydrogen blends as sustainable fuels and their impact on thrust, efficiency, and emissions, particularly the trade-offs associated

Table 3
Performance parameters of the SOFC used in the hybrid SOFC-GT system.

Parameter	SOFC	Units
\dot{W}_{SOFC}	985	kW
$\dot{Q}_{SOFC,add}$	1527	kW
η_{th}	65.50	%
η_{el}	54.75	%
Operating voltage	0.8052	V
Total voltage lost	0.2698	V
Power density	0.4026	W/cm ²
Weight flow of H ₂ used	12.77	g/s

with varying hydrogen content. The Section 2 investigates the effect of flight altitude and Mach number on the performance of the hybrid SOFC-GT system, keeping other parameters fixed. This study is critical to understanding how operational conditions, such as air density and temperature, influence both the thermodynamic and aerodynamic performance of the system, as well as the implications for fuel consumption and emissions at different cruising altitudes and speeds. The Section 3 examines the impact of equivalence ratio on the performance characteristics of the hybrid system. These parameters are pivotal in determining combustion stability, thermal efficiency, and emissions, particularly given the variability in combustor dynamics and the need to optimise system performance under realistic operational constraints. Finally, the Section 4 explores the influence of fan pressure ratio and bypass ratio on the overall performance of the hybrid SOFC-GT system. This investigation addresses the aerodynamic design considerations of the fan and bypass system, which significantly affect thrust production, fuel efficiency, and noise emissions, thereby offering insights into the hybrid system's adaptability to different propulsion requirements. By systematically addressing these parameters, the study provides a detailed evaluation of the hybrid SOFC-GT system's performance and emissions across a range of operational and design scenarios, highlighting the potential for optimisation and the feasibility of integrating such systems into future aviation technologies.

3.1. Comparison between turbofan engine and solid oxide fuel cell-gas turbine system for various NH₃/H₂ blends

We begin our analysis by comparing the performance of the hybrid SOFC-GT system with that of the conventional GT propulsion system. For the hybrid configuration, we present results across five fuel cases, with hydrogen content in the fuel mixture varying from 0% to 100%: specifically, 0% (pure ammonia), 10%, 25%, 40%, and 100% (pure hydrogen). Each of these hybrid cases is compared to the

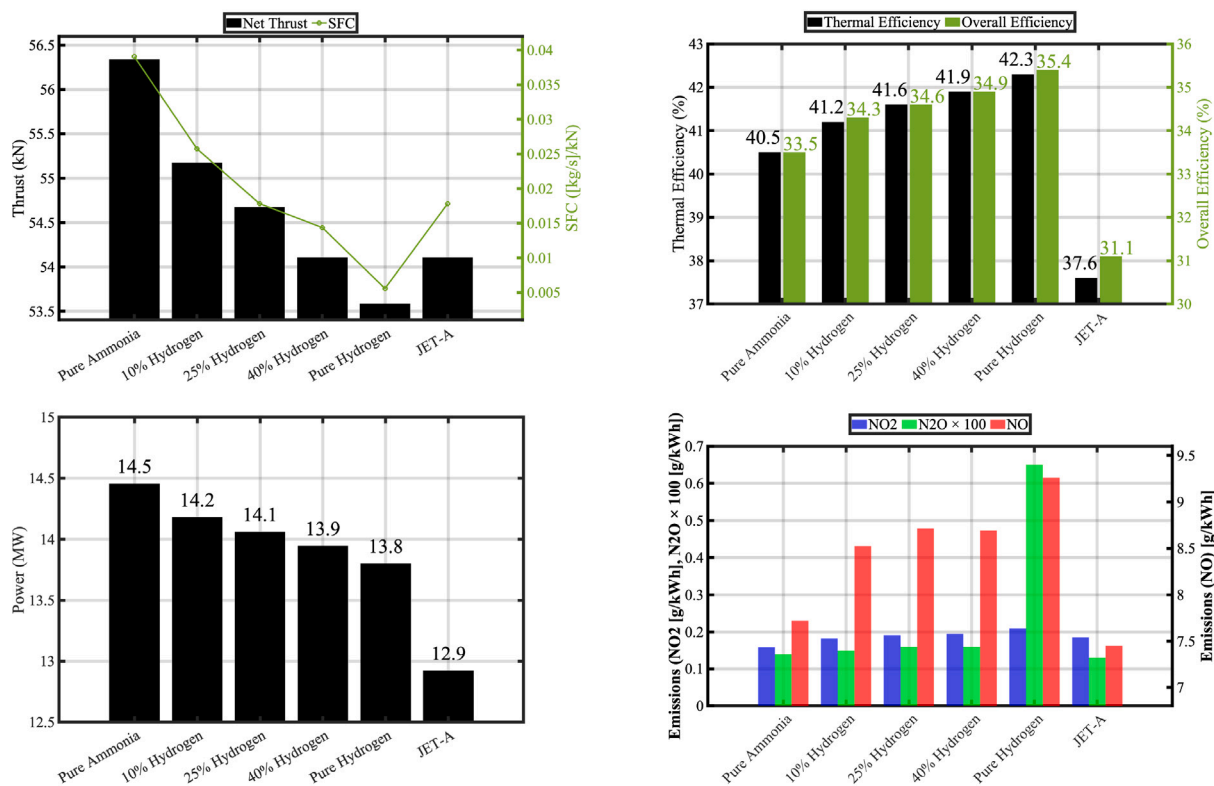


Fig. 4. Variation of net thrust (kN), specific fuel consumption (kg/(kNs)), thermal and overall efficiency, emissions (g/kWh) and power (MW) for the five cases of ammonia/hydrogen fuel blends (0%, 10%, 25%, 40%, 100% hydrogen) in the hybrid SOFC-GT system, compared with the conventional GT system fuelled by Jet A.

conventional GT system fuelled by Jet A. In all cases examined – both for the hybrid and conventional turbofan engine systems – the turbine inlet temperature was held constant at 1388.88 K (2500 R). This constant turbine inlet temperature ensures consistency with the conditions under which the JT9D turbofan model was validated, as outlined in Section 2.2.1. Additionally, the airflow through the combustor was kept constant, aligning with the validated model conditions. Due to differences in the physical properties of the fuels, maintaining a constant turbine inlet temperature necessitated adjusting the fuel mass flow rate for each case. Specifically, for the 0% hydrogen case (pure ammonia), the fuel mass flow rate was 2.2 kg/s, whereas at 100% hydrogen, this rate decreased by 86% to 0.3 kg/s. For the conventional GT system using Jet A, the fuel mass flow rate was 0.97 kg/s, representing a 56% reduction compared to the pure ammonia case in the hybrid system.

The variation in mass flow rates is attributable to the differing lower heating values (LHV) of the fuels: 18.6 MJ/kg for ammonia, 120 MJ/kg for hydrogen, and 43 MJ/kg for Jet A. Multiplying the LHVs by the corresponding fuel mass flow rates yields comparable input energy levels for all three fuels—40.9, 35.9, and 41.5 MJ/s for ammonia, hydrogen, and Jet A, respectively. The variation in mass flow rates among these fuels significantly affects the net thrust, as shown in Fig. 4. This figure illustrates that as hydrogen is progressively added to an ammonia-based fuel blend, the net thrust decreases in alignment with the reduced fuel mass flow rate. Since net thrust depends on both the mass flow rate and exhaust gas velocity, if the latter remains relatively constant, net thrust will primarily vary with changes in mass flow rate. Thus, when transitioning from ammonia to hydrogen, the reduction in fuel mass flow rate directly leads to a decrease in net thrust. Specific fuel consumption (SFC) follows a similar trend to fuel mass flow rate, gradually decreasing as hydrogen content increases from 0% to 100%. For Jet A, SFC becomes comparable to that of an ammonia/hydrogen mixture with a 60/40 ratio, thereby explaining the similar net thrust values between the two fuel types.

The differences in mass flow rates influence the thermal efficiency, as shown in Fig. 4, although the overall impact remains relatively

modest. Specifically, for pure ammonia, the thermal efficiency reaches 40.5%. As hydrogen is progressively added, a moderate increase in thermal efficiency is observed, culminating in a 4.5% improvement for pure hydrogen, corresponding to a value of 42.3%. This moderate increase in thermal efficiency when transitioning from pure ammonia to pure hydrogen is attributed to the interplay of two factors: (i) the reduction of the net thrust (4.5%), tending to lower the thermal efficiency and; (ii) a reduction in fuel mass flow rate leading to a 13% decrease in heat of combustion, which enhances the thermal efficiency. In contrast, when comparing the case of Jet-A against that of ammonia, the moderate decrease in fuel mass flow rate leads to a 1.4% increase in heat of combustion and a 4% reduction in net thrust, both of which adversely impact the thermal efficiency. Consequently, the thermal efficiency decreases by 7.3% compared to the pure ammonia case. Differences in propulsive efficiency across the various fuels are minimal, not exceeding 0.3%. Therefore, the primary driver of the observed differences in overall efficiency is the thermal efficiency. This explains why the overall efficiency follows the same qualitative and quantitative trends as the thermal efficiency across the different fuels.

In terms of total power generation, ammonia demonstrates the highest value, reaching 14.5 MW. The addition of hydrogen results in a gradual decline in total power, with a maximum reduction of 4.5%, corresponding to 13.8 MW for pure hydrogen. This reduction in total power is directly linked to the decrease in net thrust. Total power is defined as the sum of the turbine and compressor power, the engine's power output as useful mechanical energy imparted to the system (calculated as the product of net thrust and aircraft velocity), and the power generated by the SOFC. In all cases, the turbine and compressor contributions effectively balance each other, leaving the total power predominantly influenced by the latter two terms. For the hybrid system, the power output of the SOFC remains constant regardless of the fuel used. Consequently, the total power is primarily governed by the engine's mechanical power output, which, at a fixed aircraft velocity, is directly proportional to the net thrust. Thus, the

observed decrease in total power when transitioning from ammonia to pure hydrogen (4.5%) aligns closely with the reduction in net thrust (4.8%). For Jet-A, the total power is significantly lower, not only due to its reduced thrust compared to ammonia but also because of the absence of SOFC power contribution.

For pure ammonia, NO emissions are measured at 7.7 g/kWh. As hydrogen is progressively added to the fuel mixture, NO emissions gradually increase, reaching 9.3 g/kWh for pure hydrogen. A similar trend is observed for NO₂ and N₂O emissions, which rise from 0.16 and 0.0014 g/kWh, respectively, for pure ammonia, to 0.21 and 0.0065 g/kWh, respectively, for pure hydrogen. Given that the turbine inlet temperature is maintained constant in all cases, this increase in NO, NO₂, and N₂O emissions during the transition from pure ammonia to pure hydrogen may appear counterintuitive, as flame temperature – a primary driver for NO_x and N₂O formation – remains unchanged. However, this increase can be attributed to changes in combustion chemistry and reaction kinetics induced by hydrogen addition. Hydrogen enhances the production of reactive radicals such as H, O, and OH due to its higher reactivity, which in turn promotes reaction pathways that increase the formation of NO, NO₂, and N₂O from both atmospheric and fuel-bound nitrogen. In comparison, Jet-A produces lower NO_x and N₂O emissions than both ammonia and hydrogen. However, Jet-A combustion also results in significant CO₂ and CO emissions (283.03 and 0.000655 g/kWh, respectively), which are absent when using ammonia or hydrogen as fuels.

Despite the many advantages previously discussed, the practical deployment of SOFC-GT systems often encounters challenges associated with system weight, which impacts installation feasibility, operational efficiency, and structural requirements. To facilitate the adoption of SOFC-GT systems, particularly in aerospace applications where weight constraints are critical, it is imperative to identify and mitigate the weight contributions of various system components. In the hybrid SOFC-GT system analysed in this study, the total system weight was calculated as the sum of the JT9D engine (in its heaviest configuration), the SOFC, and additional components such as heat exchangers and balance of plant (BOP) equipment.

For the SOFC weight, two weight-to-power ratio estimates from prior studies were considered: a 2015 estimate of 0.263 kW/kg and a projected 2030 estimate of 0.6838 kW/kg [43,44]. The 2030 SOFC weight estimate is based on the projected weight-to-power (WtP) ratio originally referenced in Valencia et al. [44] and used in Ji et al. [43], with the projection itself derived from Guynn et al. [45]. While the primary focus is on the 2015 ratio to assess feasibility with present technology, the inclusion of the 2030 projection provides a forward-looking perspective on how advancements in SOFC materials and designs could mitigate current weight challenges. With the SOFC power output fixed at 1001 kW in the current study, these estimates correspond to SOFC weights of 3806.08 kg (2015 estimate) and 1463.88 kg (2030 projection). An additional 15% weight was assumed for heat exchangers and BOP components, while the weight contribution of decomposition reactors was deemed negligible, as internal reforming significantly reduces the need for external reformers. The total weight of the hybrid SOFC-GT system was compared to that of the conventional JT9D engine to assess its relative feasibility for aerospace applications.

The results of the weight analysis are presented in Table 4. As shown, the weight increase for the 2015 estimate is significant, amounting to 118.81% compared to the conventional JT9D engine. Even with the 2030 projections, which assume considerable advancements in SOFC technology, the weight increase remains substantial at 54.93% relative to the baseline scenario. These findings underscore the importance of ongoing improvements in the power-to-weight ratio of SOFCs to enhance their viability for aerospace applications. While the projected reductions in SOFC weight by 2030 represent a step towards more efficient systems, the weight penalty associated with integrating SOFC-GT technology into commercial aviation remains a critical barrier. This highlights the need for a multifaceted approach

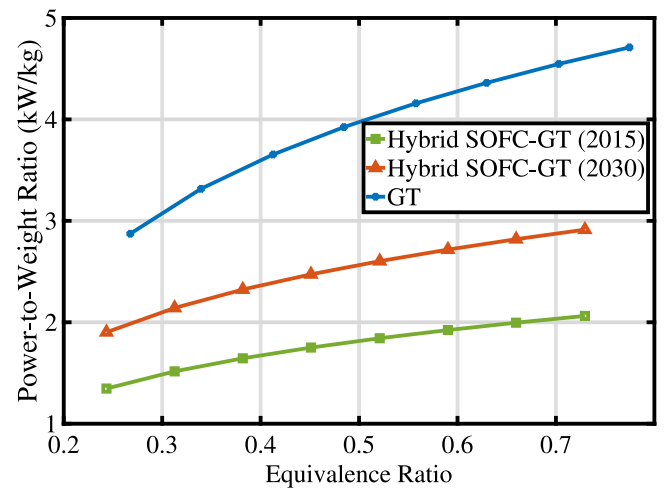


Fig. 5. Variation of the power-to-weight (PtW) ratio as a function of equivalence ratio for the turbofan engine (GT), and the hybrid SOFC-GT system based on two SOFC weight estimates [43–45].

to reduce system weight. Potential avenues include advancements in SOFC materials, such as the development of lightweight ceramic composites, and the optimisation of heat exchanger designs to minimise mass without compromising thermal efficiency. Additionally, internal reforming strategies could further reduce the need for ancillary components, such as external decomposition reactors, thereby contributing to overall weight savings. Moreover, system-level optimisations, including the integration of hybrid configurations tailored to specific aircraft mission profiles, may help mitigate the weight challenges while maximising the efficiency benefits of SOFC-GT systems. These strategies, coupled with continued research and development in manufacturing technologies and material science, are essential to ensure that SOFC-GT systems become a competitive alternative to conventional gas turbines in commercial aviation.

The weight calculations discussed earlier gain greater significance when analysed alongside the power produced by the system, specifically through the power-to-weight (PtW) ratio. For this purpose, the PtW ratio of the hybrid SOFC-GT system (based on both the 2015 and 2030 SOFC weight estimates) and the conventional turbofan engine has been evaluated as a function of the equivalence ratio, with the results presented in Fig. 5. For the hybrid system, a 90/10 ammonia/hydrogen fuel blend was used. Based on the 2015 SOFC weight estimate, the PtW ratio of the hybrid system varies between 1.35 kW/kg at the fuel-lean end ($\phi = 0.24$) and 2.1 kW/kg near stoichiometric conditions ($\phi = 0.77$). Using the more optimistic 2030 SOFC weight estimate, the PtW ratio increases significantly, ranging from 1.9 to 2.97 kW/kg over the same equivalence ratio range, representing a 41% improvement. Despite this improvement, even under the optimistic 2030 scenario, the PtW ratio of the hybrid SOFC-GT system remains considerably lower than that of the conventional turbofan engine, whose PtW ratio ranges from 2.7 to 4.7 kW/kg over the same equivalence ratio values. This translates to a PtW ratio for the hybrid system that is between 30% and 37% lower than that of the turbofan engine under identical operating conditions. The higher PtW ratio of the turbofan engine reflects its inherently optimised design for power generation and weight efficiency, attributes that remain challenging for hybrid systems to match given the current state of SOFC technology. These findings underscore the critical need for continued advancements in fuel cell technology, particularly in reducing the weight of SOFC stacks and associated balance-of-plant components.

Table 4
Weight comparison between the turbofan engine and the hybrid SOFC-GT system, using two SOFC weight estimates.

Components	Turbofan	SOFC-GT _{2015 estimate}	SOFC-GT _{2030 estimate}
JT9D engine	4216 kg	4216 kg	4216 kg
SOFC (1001 kW)	–	3806.08 kg [43–45]	1463.88 kg [43–45]
Heat exchangers and BOP	–	1203.31 kg	851.98 kg
Total	4216 kg	9225.39 kg	6531.86 kg
Δ Weight increase	–	118.81%	54.93%

3.2. Influence of flight altitude and mach number

Understanding the influence of flight altitude and Mach number on the performance metrics of the hybrid SOFC-GT system fuelled by ammonia–hydrogen is essential for evaluating its feasibility and optimising its operation in real-world aviation scenarios. Flight altitude and Mach number are critical parameters that significantly affect atmospheric conditions such as pressure, temperature, and air density, which in turn impact the thermodynamic processes within the engine and fuel cell system. Analysing how these variables influence the hybrid system's efficiency, thrust output, fuel consumption, and emissions is crucial for designing propulsion systems that can maintain optimal performance across the diverse operating conditions encountered during flight. While some of the conditions studied may not have direct practical applications in aviation, their inclusion allows for a comprehensive understanding of the system's behaviour across a wide range of operating envelopes. This approach provides valuable insights into how the hybrid SOFC-GT system responds to extreme or boundary conditions, which can inform system design, safety margins, and optimisation strategies. By encompassing a broader spectrum of conditions, the analysis ensures robustness and highlights trends that may otherwise be overlooked if only typical operating points were considered. This section aims to elucidate the operational envelope of the hybrid SOFC-GT system, identify potential performance limitations at various altitudes and speeds, and provide insights into the system's adaptability and robustness. The analysis considers altitudes ranging from 0 to 10.36 km and Mach numbers from 0.1 to 0.8, with a fuel mixture composed of 10% hydrogen and 90% ammonia (on a mole fraction basis). The results of this analysis are summarised in Fig. 6. Such an analysis not only contributes to the advancement of sustainable aviation technologies but also aids in bridging the gap between theoretical designs and practical implementation in the aerospace industry.

As shown in Fig. 6, the net thrust increases with altitude and decreases with Mach number. Specifically, the net thrust ranges from a maximum of 90 kN (at a Mach number of 0.1 and an altitude of 10.36 km) to a minimum of 49 kN (at a Mach number of 0.8 and sea level). This trend can be understood by recognising that net thrust is the difference between gross thrust and ram thrust. At a constant altitude and fuel flow, gross thrust increases with Mach number because the higher flight velocity increases the air mass flow rate into the engine, thereby raising the exhaust mass flow rate and momentum thrust. For instance, at 10.36 km, gross thrust increases from 99 kN at Mach 0.1 to 128 kN at Mach 0.8, representing a 29% increase. Simultaneously, ram thrust also increases due to the higher velocity and mass flow rate of incoming air. However, the growth in ram thrust is far more pronounced than that of gross thrust; in the same example, ram thrust increases from 9 kN at Mach 0.1 to 73 kN at Mach 0.8, a 700% increase. This significant rise in ram thrust outweighs the increase in gross thrust, resulting in a net decrease in the overall thrust as Mach number increases. Regarding altitude, at a constant Mach number and fuel flow, gross thrust decreases with increasing altitude due to the reduction in air density, which leads to a lower air mass flow rate. For instance, at Mach 0.8, gross thrust decreases from 132 kN at sea level to 128 kN at 10.36 km, a 3% reduction. Similarly, ram thrust decreases with altitude as it is directly proportional to the air mass flow rate. In the same example, ram thrust drops from 83 kN at sea level to 73 kN at 10.36 km, a 12% decrease. Because the decrease in ram thrust is

greater than that of gross thrust, the resulting net thrust increases with altitude. For instance, the net thrust rises from 49 kN at sea level to 55 kN at 10.36 km, an 11% increase.

SFC varies between 0.0158 (kg/s)/kN at Mach 0.1 and 10.36 km altitude and 0.0291 (kg/s)/kN at Mach 0.8 and sea level. The average SFC across all conditions is 0.0215 (kg/s)/kN, with a standard deviation of 0.00376 (kg/s)/kN. The variation in SFC is inversely proportional to the net thrust, as SFC is defined as the ratio of fuel flow to net thrust. Since the fuel flow remains constant under all conditions, variations in SFC are entirely governed by changes in net thrust. Accordingly, SFC attains its highest value under minimum net thrust conditions and its lowest when net thrust is maximised.

The overall power varies between 3695 MW at Mach 0.1 and 10.36 km altitude, and 14,394 MW at Mach 0.8 and sea level. The mean overall power across the entire operational envelope is 9956 MW, with a standard deviation of 3461 MW. At a typical cruising altitude and speed for the JT9D engine – 10.36 km and Mach 0.8 – the overall power reaches 14,221 MW, which is slightly less than 1.2% below the maximum recorded value. The overall power decreases with increasing altitude at a constant Mach number and increases with increasing Mach number at a constant altitude. Since the power from the SOFC remains constant and the turbine and compressor power contributions balance each other under all conditions, the overall power is primarily influenced by changes in the useful propulsive power, which depends on the flight velocity and net thrust. When altitude increases at a constant Mach number, the flight velocity decreases. For example, at Mach 0.8, increasing the altitude from sea level to 10.36 km reduces the velocity from 272.3 m/s to 238.7 m/s, a 12.34% decrease. Simultaneously, the net thrust increases, rising from 49 kN to 55 kN, a 12.83% increase. While these percentage changes appear to offset each other, their combined effect results in a slight decrease in propulsive power, which drives the overall power downward. Conversely, at a constant altitude, increasing the Mach number leads to a significant rise in flight velocity and a moderate reduction in net thrust, resulting in a much more pronounced increase in propulsive power. For instance, at an altitude of 10.36 km, increasing the Mach number from 0.1 to 0.8 raises the flight velocity from 30 m/s to 239 m/s (a 700% increase) while reducing the net thrust from 90 kN to 55 kN (a 39% decrease). This dominant increase in flight velocity outweighs the reduction in net thrust, leading to a substantial rise in overall power.

The thermal efficiency ranges from 41.2% (at 10.36 km, Mach 0.8) to 54.5% (at sea level, Mach 0.1), with an average value of 45% and a standard deviation of 3%. The results indicate that thermal efficiency decreases with either increasing altitude or increasing Mach number. This behaviour can be understood by considering that thermal efficiency is a function of propulsive power, exhaust kinetic power, and bypass kinetic power, assuming that other terms in the denominator of the thermal efficiency equation remain relatively constant. For example, at a constant altitude of 10.36 km, increasing the Mach number from 0.1 to 0.8 results in the following changes: (i) propulsive power increases by 284%, driven by the factors previously discussed in the context of overall power; (ii) exhaust kinetic power decreases by 67%, primarily due to the higher flight velocity; and (iii) bypass kinetic power decreases by 92%, also a result of the increased flight velocity. While the significant rise in propulsive power tends to enhance thermal efficiency, the reductions in exhaust and bypass kinetic power exert a stronger negative influence, leading to a net decrease in thermal

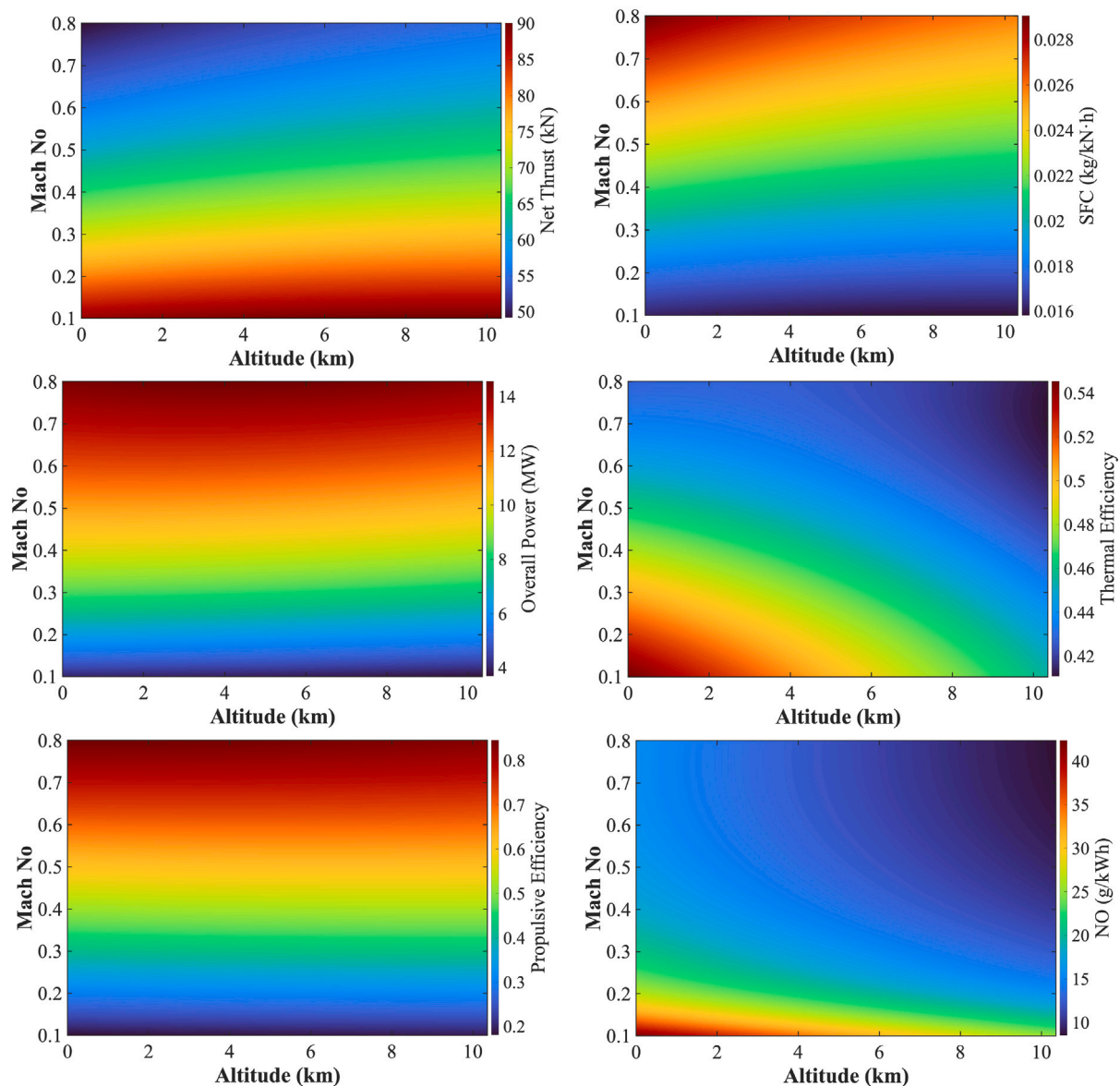


Fig. 6. The variation of net thrust (kN), specific fuel consumption (kg/kN h), thermal efficiency, propulsive efficiency, overall power (MW) and specific NO emissions (g/kWh) as a function of altitude and Mach number.

efficiency of 10%. At a constant Mach number with varying altitude, the response of thermal efficiency reflects a more complex interplay of system parameters. For instance, at Mach 0.8, increasing the altitude from 5.18 km to 10.36 km reduces the thermal efficiency from 42.6% to 41.2%, a 3.1% decrease. Under these conditions, the key terms influencing thermal efficiency respond as follows: (i) propulsive power decreases by 2%, as previously explained in the discussion of overall power; (ii) exhaust kinetic power increases by 14%, largely due to the reduction in flight velocity; and (iii) bypass kinetic power decreases by 13%, resulting from proportional decreases in both flight velocity and the bypass air exhaust velocity. Here, the combined negative effects of reduced propulsive power and bypass kinetic power outweigh the positive contribution of increased exhaust kinetic power, thereby leading to a net reduction in thermal efficiency.

Propulsive efficiency exhibits a wide range, varying from 18.1% (at sea level, Mach 0.1) to 84.6% (at sea level, Mach 0.8), with only minimal changes observed at a constant Mach number. For instance, at Mach 0.8, the propulsive efficiency changes by less than 2% as altitude increases from sea level to 10.36 km. Specifically, at Mach 0.8 and an altitude of 10.36 km, propulsive efficiency reaches 83.1%, whereas at

a lower altitude of 8.29 km and Mach 0.6, it decreases to 70%. As illustrated in Fig. 6, propulsive efficiency is primarily influenced by Mach number, with altitude playing only a secondary role. For example, when the Mach number increases from 0.1 to 0.8 at an altitude of 10.36 km, the following effects are observed: (i) propulsive power increases by 284%, driven by the significantly higher flight velocity; (ii) exhaust kinetic power decreases by 67% as a result of the increased flight velocity reducing the relative energy loss in the exhaust stream; and (iii) bypass kinetic power decreases by 92%, also due to the higher flight velocity and its impact on bypass air dynamics. These combined changes collectively enhance propulsive efficiency, highlighting the dominant role of Mach number in its variation.

Specific NO emissions, influenced by variations in both the mass of NO and the overall power, range from 8.5 g/kWh (Mach 0.8, 10.36 km) to 42.4 g/kWh (Mach 0.1, sea level), with higher values generally observed at lower Mach numbers. This behaviour can be explained by considering the relationship between altitude, Mach number, and NO formation. Mass-based NO emissions are generally higher at low altitudes because of the increased air density and higher oxygen availability, which enhance the combustion process and the

formation of nitrogen oxides. Additionally, the higher temperatures and pressures within the combustor at lower altitudes promote the thermal NO_x formation pathway, governed by the extended Zeldovich mechanism. These factors result in greater NO production, particularly at low Mach numbers, where the overall airflow and combustion temperatures further amplify these effects. Simultaneously, as discussed earlier, the overall power increases significantly with Mach number due to the higher flight velocity and propulsive power, while altitude has only a negligible effect on overall power. The interplay of these factors—higher NO production at low Mach numbers and increasing overall power with Mach number—leads to the trends observed in Fig. 6. Specifically, at low Mach numbers, the higher mass-based NO production dominates, leading to elevated specific NO emissions. Conversely, at higher Mach numbers, the increase in overall power outpaces the slower rise in NO mass production, resulting in lower specific NO emissions. This synergistic relationship between NO formation and power output underscores the critical role of operational parameters in determining the emissions characteristics of the engine.

3.3. Influence of equivalence ratio

The equivalence ratio is a pivotal parameter in the design and optimisation of hybrid SOFC-GT systems, as it directly influences key performance metrics. By determining the air-to-fuel mixture in the combustor, the equivalence ratio affects combustion efficiency, flame stability, and temperature profiles, ultimately shaping the system's overall performance. For an emerging technology that integrates a SOFC with a gas turbine, maintaining an appropriate equivalence ratio is critical to maximising fuel utilisation and achieving environmentally compliant emissions, particularly given the unique combustion characteristics of ammonia-hydrogen fuel blends. This section explores the influence of equivalence ratio on the hybrid SOFC-GT system's performance, providing insights that can guide design and operational strategies to enhance efficiency, reduce emissions, and ensure the viability of this sustainable propulsion technology. The analysis focuses on the same six key quantities that were investigated in the previous section, i.e., net thrust, SFC, thermal and propulsive efficiency, overall power and specific NO emissions. The only input parameter that changes is the equivalence ratio varying between 0.24 and 0.8. All the results related to the effect of the equivalence ratio are summarised in Fig. 7.

The net thrust varies between 50.6 and 85.0 kN, with an average value of 70.7 kN, and increases with the equivalence ratio following a logarithmic relationship: $y = 27.769 \ln(x) + 90.422$, where y is the net thrust and x is the equivalence ratio. The coefficient of determination (R^2) for this function is 0.9998, indicating an almost perfect fit. This dependence is physically reasonable, as net thrust is governed by the total mass flow rate and the exhaust velocity, both of which increase with the equivalence ratio. An increase in equivalence ratio raises the proportion of fuel to air, introducing more chemical energy into the combustion chamber. This leads to a hotter and more energetic combustion process, elevating the temperature and pressure at the combustor exit and consequently increasing the turbine inlet temperature. The additional energy available for expansion through the turbine and nozzle accelerates the exhaust gases to higher velocities. At constant flight velocity, the incoming air mass flow remains unchanged, but the exhaust gases, now carrying more kinetic energy, generate a larger momentum surplus. This surplus directly contributes to the higher net thrust. In essence, increasing the equivalence ratio enhances the thermal energy in the engine's core flow, which is subsequently converted into greater exhaust kinetic energy. This improved momentum exchange between the engine and the surrounding air results in a significant increase in net thrust, underscoring the critical role of equivalence ratio in optimising engine performance.

The relationship between SFC and the equivalence ratio is nearly perfectly linear, as described by the equation $y = 0.0551x + 0.0225$,

where y is the SFC and x is the equivalence ratio. The coefficient of determination ($R^2 = 0.9989$) indicates an excellent fit. SFC values range from 0.0352 to 0.0655 kg/kN h, with an average of 0.0510 kg/kN h. As the equivalence ratio increases, the proportion of fuel relative to air rises, introducing more fuel into the combustion chamber per unit mass of air. While net thrust also increases with equivalence ratio, it does so at a slower rate because the thrust gain is primarily influenced by changes in exhaust velocity and momentum rather than by the total air mass flow. This results in the fuel consumption growing more rapidly than thrust, causing a near-linear increase in SFC, which is defined as the ratio of fuel flow to net thrust. Physically, the additional fuel increases the chemical energy input to the system, raising turbine inlet temperatures and enhancing exhaust velocities, which contributes to increased thrust. However, the incremental thrust gain per unit of additional fuel diminishes as more fuel is added, reflecting diminishing returns. Consequently, under conditions of constant flight velocity and other fixed parameters, this imbalance between fuel flow and thrust translates into the observed linear rise in SFC.

Fig. 7 illustrates the effect of equivalence ratio on thermal efficiency, which varies between 0.277 and 0.437, with an average value of 0.349. The relationship between thermal efficiency and equivalence ratio is described by the exponential equation $y = 0.2572x^{-0.379}$, with a coefficient of determination (R^2) of 0.9989, indicating an excellent fit. To explain the observed response of thermal efficiency to changes in equivalence ratio, two representative cases are considered: an equivalence ratio of 0.24 (thermal efficiency of 0.44) and 0.73 (thermal efficiency of 0.29). Increasing the equivalence ratio from 0.24 to 0.73 results in a 34% decrease in thermal efficiency. This decline can be understood by analysing the behaviour of the individual terms contributing to the thermal efficiency. For the useful power output, as the equivalence ratio increases from 0.24 to 0.73: (i) Propulsive power increases by 60%, driven by the rise in net thrust as previously discussed. (ii) Bypass kinetic power and the fuel cell's useful power both remain nearly unchanged. (iii) Exhaust kinetic power increases significantly, by 266%, due to the elevated velocity of the exhaust gases. Despite the significant increase in bypass kinetic power, the useful power output is predominantly influenced by propulsive power, which accounts for 78% of the useful power at an equivalence ratio of 0.24 but drops to 69% at 0.73. Simultaneously, for the total power input, the following changes occur: (i) Power from the chemical energy of the fuel increases by 179%, primarily due to the higher fuel flow. (ii) Power from electrochemical processes in the fuel cell decreases by 13%. (iii) Power associated with fuel decomposition remains largely unchanged. The total power input is dominated by the chemical energy of the fuel, accounting for 96% of total input at an equivalence ratio of 0.24, increasing to 99% at 0.73. Although both the useful power output and total power input increase with equivalence ratio, the more pronounced rise in total power input, driven by the increased fuel availability, leads to a net reduction in thermal efficiency.

Propulsive efficiency exhibits a linear relationship with the equivalence ratio, described by $y = -0.2327x + 0.8971$, with an R^2 value of 0.9979, indicating an excellent fit. Similar to thermal efficiency, propulsive efficiency decreases as the equivalence ratio increases. It ranges from 0.843 at an equivalence ratio of 0.24 to 0.714 at 0.73, with an average value of 0.776. However, the drop in propulsive efficiency is less pronounced than that of thermal efficiency; from 0.24 to 0.73, propulsive efficiency decreases by 15%, compared to a 37% reduction in thermal efficiency. The decrease in propulsive efficiency with increasing equivalence ratio can be attributed to changes in the propulsive power and exhaust kinetic power. Both terms increase as equivalence ratio rises, but propulsive power, being the dominant contributor to propulsive efficiency, increases only moderately. This moderate increase results in the observed decline in propulsive efficiency.

As shown in Fig. 7, the overall power exhibits a logarithmic relationship with the equivalence ratio, described by $y = 6.6309 \ln(x) + 2.598$,

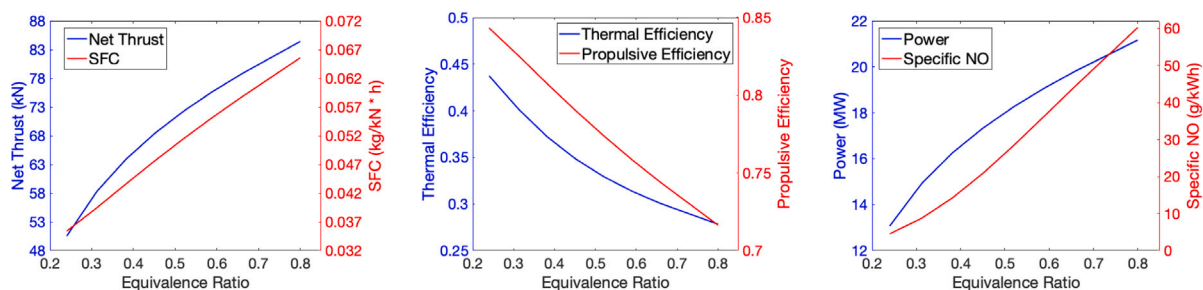


Fig. 7. The variation of net thrust (kN), specific fuel consumption (kg/kN h), thermal efficiency, propulsive efficiency, overall power (MW) and specific NO emissions (g/kWh) as a function of the equivalence ratio.

with an R^2 value of 0.9998, indicating an excellent fit. The overall power ranges from 13.13 MW at an equivalence ratio of 0.24 to 21.12 MW at 0.8, with an average value of 17.88 MW. This response is primarily driven by changes in propulsive power, as the contributions of the remaining terms to the overall power are negligible. The increase in propulsive power is directly linked to the rise in net thrust, which is governed by the increase in gross thrust. The gross thrust grows due to the elevated exhaust velocity and mass flow rate resulting from the higher equivalence ratio, while the ram thrust remains nearly constant at the given flight conditions. Consequently, the overall power mirrors the qualitative response of net thrust to the equivalence ratio, reflecting the dominant influence of thrust-related dynamics in determining the system's performance under these conditions.

Specific NO emissions exhibit a weakly non-linear response to changes in equivalence ratio, which is well-described by a second-degree polynomial: $y = 64.934x^2 + 37.297x - 8.8187$, with an R^2 value of 0.999, indicating an excellent fit. Specific NO values range from 3.87 g/kWh at an equivalence ratio of 0.24 to 62.58 g/kWh at 0.8, with an average value of 29.9 g/kWh. The observed behaviour arises from the interplay between the increase in NO production and the corresponding increase in overall power as the equivalence ratio rises. As the equivalence ratio approaches stoichiometric conditions, the combustion temperature increases significantly, enhancing the thermal NO formation pathway governed by the extended Zeldovich mechanism. This mechanism becomes increasingly efficient at higher temperatures, leading to a rapid escalation in NO emissions. However, the overall power does not increase at the same rate as NO production, as its growth is primarily influenced by the moderate increase in net thrust and propulsive power, which scale logarithmically with equivalence ratio. This disparity between the rates of increase in NO emissions and overall power leads to the weakly non-linear response of specific NO. The non-linearity becomes more pronounced at higher equivalence ratios, reflecting the system's sensitivity to elevated combustion temperatures and the thermochemical kinetics driving NO formation. These findings underscore the critical need to balance equivalence ratio adjustments with emissions considerations, particularly as the system approaches stoichiometric conditions where NO formation accelerates.

3.4. Influence of fan pressure ratio and bypass ratio

The fan pressure ratio (FPR) and bypass ratio (BPR) are fundamental parameters that define the aerodynamic and thermodynamic architecture of a turbofan engine. Their combined influence extends across nearly every facet of engine performance, from the efficiency of energy conversion to the character and magnitude of the thrust produced. The FPR, which determines the compression level of the bypass airflow, is analysed in this study within the range of 1.0 to 2.0. This range is selected to reflect realistic operational limits while ensuring that the fan retains its primary function. Beyond this range, the fan would effectively operate as a compressor, deviating from its intended aerodynamic role. Similarly, the BPR, which dictates the proportion of airflow bypassing the engine core versus that passing through it,

is examined across a range of 1.5 to 10.5. This range encompasses typical turbofan designs while addressing the trade-offs between fuel efficiency, noise reduction, and specific thrust. While these ranges provide a comprehensive framework for analysis, it is important to note that not all combinations of FPR and BPR within the examined ranges could be evaluated. Specifically, for high values of both parameters, numerical limitations constrained the solver's ability to converge to a valid solution. This resulted in a subset of the parametric domain being excluded from the plots. These blank regions, particularly visible in the upper-right corners of the contour plots in Fig. 8, should not be interpreted as areas of low performance or zero values, but rather as configurations beyond the current model's numerical stability limits.

Investigating these parameters is essential for understanding and optimising the performance of the hybrid SOFC-GT system. This analysis will systematically examine how variations in FPR and BPR influence six key performance metrics previously studied: net thrust, SFC, thermal efficiency, propulsive efficiency, overall power, and specific NO emissions. By evaluating these critical quantities, we seek to provide a detailed understanding of how these parameters govern the trade-offs between thrust generation, efficiency, and emissions.

Starting with net thrust, as shown in Fig. 8, the average value is 47.3 kN. Both the BPR and the FPR have a significant impact on net thrust, though their influence varies across the parametric space. Specifically, at low BPR (<2), the FPR has a negligible effect on net thrust because thrust production is dominated by the core flow. In these conditions, changes in FPR, which primarily influence the bypass flow, contribute minimally to the overall thrust. However, as the BPR increases, the bypass flow accounts for a larger fraction of thrust, amplifying the impact of FPR by increasing the momentum of the bypass stream. For instance, at a BPR of 5 (typical for the turbofan engine studied here), increasing the FPR from 1.2 to 1.8 results in the following: (i) ram thrust remains largely constant at 72 kN, as expected since flight speed and altitude are fixed; and (ii) gross thrust increases by 13%, from 114 to 129 kN. This increase is attributed to the higher FPR, which compresses and accelerates the bypass air more effectively, leading to a greater exit velocity. As gross thrust is proportional to the air mass flow rate and the velocity difference between the exhaust and incoming air, the higher bypass exit velocity directly enhances gross thrust. Consequently, net thrust increases by 35%, from 42 to 57 kN. When the FPR is held constant, the response of net thrust to changes in BPR also varies significantly. At low FPR values (<1.1), the BPR has minimal influence on net thrust because the bypass air velocity is close to the flight velocity, resulting in negligible momentum contribution from the bypass stream, regardless of the BPR. However, as the FPR increases, the bypass air velocity rises significantly, amplifying the thrust contribution from the bypass stream and making the bypass ratio's effect on net thrust more pronounced. At sufficiently high FPR, the BPR can have a substantial effect on net thrust. For example, at a FPR of 1.5 (typical for the JT9D engine), increasing the BPR from 3 to 7 leads to the following: (i) ram thrust increases by 106%, from 47 to 96 kN, due to the increased total mass flow rate of air entering the engine, as a higher proportion of the airflow bypasses the core;

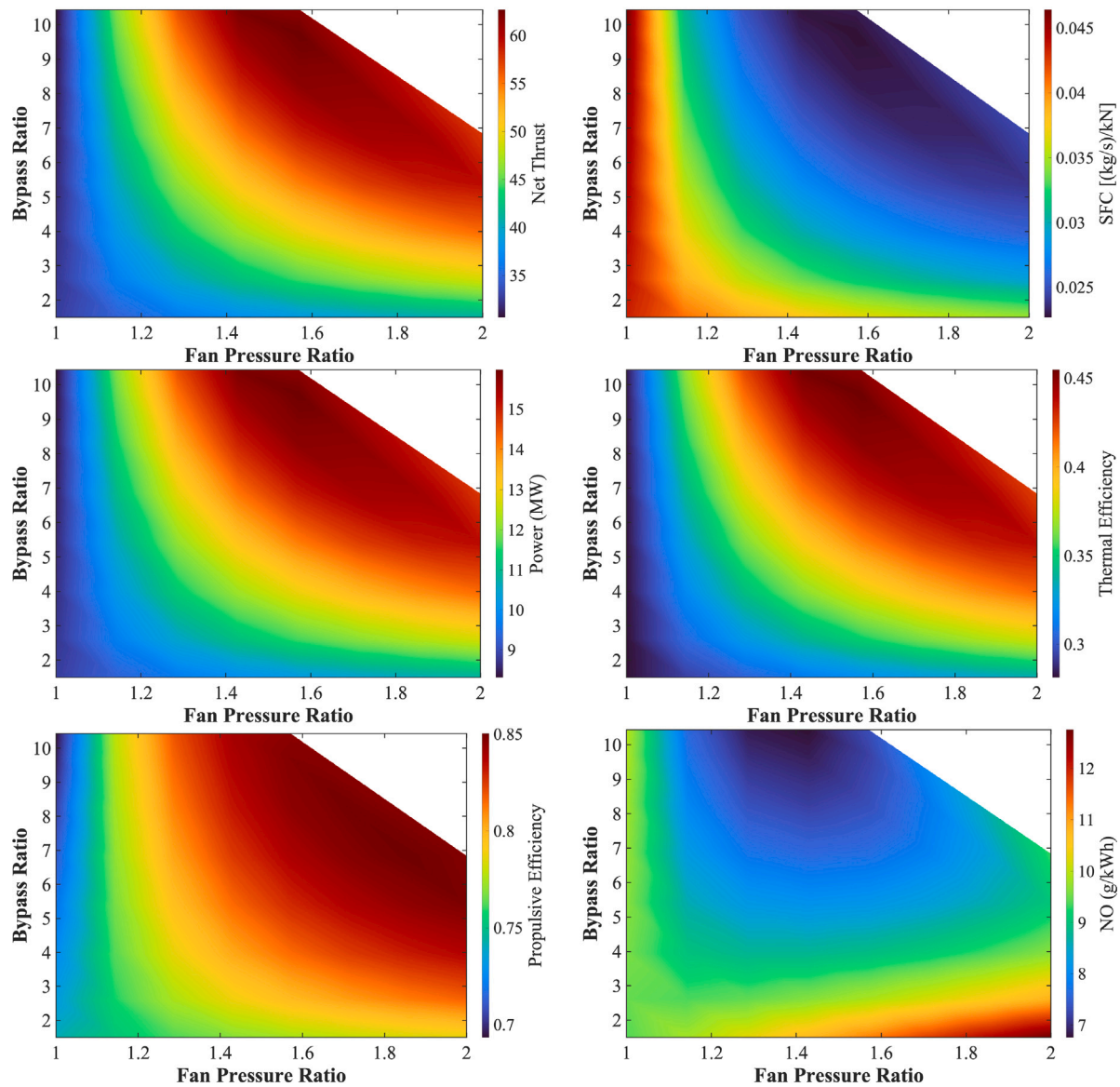


Fig. 8. The variation of net thrust (kN), specific fuel consumption (kg/kN h), thermal efficiency, propulsive efficiency, overall power (MW) and specific NO emissions (g/kWh) as a function of FPR and BPR. Note: The blank regions appearing in the upper-right corners of each subplot correspond to combinations of high FPR and BPR where the solver failed to converge due to numerical instability. These regions were therefore excluded from the analysis.

and (ii) gross thrust increases by 66%, from 92 to 153 kN, because the higher bypass air mass flow, combined with the increased bypass air velocity, significantly boosts the momentum of the bypass stream. These combined effects result in a net thrust increase of 28%, from 45 to 58 kN.

SFC is primarily governed by net thrust, as the fuel flow rate remains constant. Since SFC is inversely proportional to net thrust, it exhibits an inverse relationship with the trends described for net thrust earlier. For a BPR of 5, increasing the FPR from 1.2 to 1.8 results in a 26% decrease in SFC, from 0.034 to 0.025 (kg/s)/kN, due to the corresponding increase in net thrust. Similarly, for a FPR of 1.5, increasing the BPR from 3 to 7 leads to a 22% reduction in SFC, from 0.032 to 0.025 (kg/s)/kN, driven by the increase in net thrust associated with the higher BPR. Across the entire parametric space, the average SFC is 0.032 (kg/s)/kN. However, when focusing on the more constrained range of FPR (1.2–1.8) and BPR (3–7) values, the average SFC decreases to 0.028 (kg/s)/kN. This reduction reflects the combined influence of increasing bypass flow and higher FPR, both of which enhance net thrust, thereby improving the efficiency of fuel utilisation.

The overall power exhibits a response to FPR and BPR similar to that observed for net thrust. This is expected, as the overall power is primarily driven by changes in propulsive power, which is directly proportional to net thrust, given that the flight velocity is constant. At typical values of FPR (1.5) and BPR (5), the overall power is 13,376 kW, with 12,374 kW contributed by propulsive power and 1001 kW by the SOFC. When increasing the BPR from 3 to 7 (with FPR held constant at 1.5), the overall power increases by 25%, from 10,744 kW to 13,729 kW, closely tracking the 28% increase in propulsive power under the same conditions. Similarly, increasing the FPR from 1.2 to 1.8 (while keeping the BPR constant at 5) results in a 32% increase in overall power, from 11,069 kW to 14,631 kW, closely reflecting the 35% rise in propulsive power. This strong correlation underscores the dominant role of propulsive power in determining the overall power. Across the entire parametric space, the average overall power is 12,296 kW. However, within the more constrained range of FPR (1.2–1.8) and BPR (3–7), the average increases to 13,182 kW. This increase highlights the enhanced energy conversion achieved within these optimised design parameters, reflecting the balance between thrust generation and power efficiency in hybrid SOFC-GT systems.

The thermal efficiency varies between 0.28 and 0.45, with an average value of 0.37 across the entire parametric space. In the more constrained range of FPR values between 1.2 and 1.8 and BPR values between 3 and 7, the average thermal efficiency increases to 0.39, reflecting the favourable effects of these parameters. Thermal efficiency generally improves with increasing FPR and BPR, which is explained by analysing the changes in total useful power and total input power. At typical values of FPR (1.5) and BPR (5), the total useful power is 16,334 kW, with its distribution highlighting the dominant role of propulsive power (76%), followed by exhaust kinetic power (14%), bypass kinetic power (4%), and the SOFC power (6%). Simultaneously, the total input power is 41,568 kW, with the majority (94%) derived from the chemical energy of the fuel, 4% from electrochemical processes in the SOFC, and 2% from the energy associated with fuel decomposition. These distributions underscore the central role of propulsive power in determining total useful power and the overwhelming influence of fuel chemical energy on total input power. When the FPR increases from 1.2 to 1.8 at a constant BPR of 5, the total useful power rises by 23%, from 14,229 to 17,447 kW. This increase is driven by: (i) a 35% increase in propulsive power, the dominant contributor, due to the higher bypass air velocity and momentum; (ii) negligible changes in the SOFC power; (iii) a 26% decrease in exhaust kinetic power, as more energy is diverted to compressing the bypass airflow, reducing the energy available for the core exhaust and lowering its velocity; (iv) an 80% increase in bypass kinetic power, attributed to greater compression and acceleration by the fan, combined with the larger mass flow through the bypass duct. The combined effect of increasing propulsive and bypass kinetic powers against the decreasing exhaust kinetic power results in a net increase in total useful power. Meanwhile, the total input power decreases slightly (by 2%), primarily due to reduced contributions from electrochemical processes in the SOFC. Consequently, thermal efficiency increases proportionally to the rise in total useful power. Similarly, when the BPR increases from 3 to 7 at a constant FPR of 1.5, the total useful power increases by 20%, from 14,717 to 17,680 kW. This increase is driven by: (i) a 28% increase in propulsive power due to the higher bypass ratio, which enhances the thrust contribution from the bypass stream; (ii) negligible changes in SOFC power; (iii) a 20% decrease in exhaust kinetic power, as a larger fraction of the airflow bypasses the core, reducing the core mass flow and the energy available for the exhaust stream; (iv) a 137% increase in bypass kinetic power, driven by the substantial increase in mass flow through the bypass duct, coupled with relatively stable bypass air velocity. The combined effect of increasing propulsive and bypass kinetic powers against the decreasing exhaust kinetic power results in a net increase in total useful power by 20%. In this case, the total input power remains largely unchanged. As a result, thermal efficiency increases proportionally to the rise in total useful power.

Propulsive efficiency varies between 0.7 and 0.85, with an average value of 0.80 across the entire parametric space. It increases with both FPR and BPR, primarily driven by changes in propulsive power and, to a lesser extent, by variations in exhaust kinetic power. When the FPR increases from 1.2 to 1.8 at a constant BPR of 5, the propulsive efficiency rises by 9%, from 0.77 to 0.83. This improvement results from a 35% increase in propulsive power, which enhances the useful energy converted into thrust, and a 26% reduction in exhaust kinetic power, which minimises energy losses to the exhaust stream. Similarly, when the BPR increases from 3 to 7 at a constant FPR of 1.5, propulsive efficiency increases by 5%, from 0.79 to 0.83. This is attributed to a 28% increase in propulsive power, driven by the greater contribution of the bypass stream to thrust, and a 20% reduction in exhaust kinetic power due to the redistribution of airflow towards the bypass duct. These results highlight the dominant role of propulsive power in improving propulsive efficiency, while the reduction in exhaust kinetic power further supports the observed trend by mitigating energy losses.

Specific NO emissions, defined as the ratio of NO mass production to the overall power output, vary between 6.8 and 12.8 g/kWh,

with an average of 8.9 g/kWh across the entire parametric space. To understand the trends observed in Fig. 8, it is essential to consider how FPR and BPR influence both NO mass production and overall power independently. While the behaviour of overall power under varying FPR and BPR has been discussed previously, we now focus on the underlying mechanisms governing NO formation. The mass production of NO is primarily sensitive to the air-fuel ratio (AFR) and the thermodynamic conditions in the engine core. Increasing the FPR intensifies the pressure and temperature fields within the combustor, raising the flame temperature and accelerating thermal NO formation via the extended Zeldovich mechanism. In contrast, altering the BPR merely redistributes airflow between the core and bypass streams without significantly changing the core's temperature and pressure profiles. As a result, while increases in FPR foster NO production by enhancing core combustion temperatures, variations in BPR have a negligible effect on NO emissions since they do not substantially alter the fundamental conditions governing NO formation. Simultaneously, both FPR and BPR increments lead to increases in overall power, as previously outlined. This combination – rising NO mass production with increasing FPR and relatively stable or slightly rising overall power – shapes the observed profile of specific NO emissions illustrated in Fig. 8.

4. Conclusions

This study presented a computational investigation of a hybrid SOFC-GT propulsion system for commercial aviation using ammonia as the primary fuel. The system's performance was compared with a conventional turbofan engine, analysing the effects of key parameters such as altitude, Mach number, equivalence ratio, FPR, and BPR. NASA's T-MATS toolbox, integrated with Cantera-based chemical equilibrium calculations, enabled accurate, steady-state simulations of thermodynamic and aerodynamic interactions within the system.

Key findings include the following:

- **Comparison with Conventional Turbofan and Fuel Sensitivity:** The SOFC-GT system with ammonia - hydrogen blends demonstrated thrust and efficiency approaching those of a conventional turbofan. Pure ammonia achieved 14.5 MW total power and 2.2 kg/s fuel flow, but with higher SFC and lower thermal efficiency. Adding hydrogen reduced fuel flow by 86% at pure hydrogen, improving thermal efficiency by 4.5%, and eliminating CO₂ emissions. NO emissions increased by 20% with pure hydrogen compared to ammonia.
- **Influence of Altitude and Mach Number:** Higher altitudes generally improved net thrust and efficiency metrics. At Mach 0.8 and 10.36 km altitude, net thrust increased by 11% to 55 kN compared to 49.5 kN at sea level. Increasing Mach number from 0.1 to 0.8 at 10.36 km altitude resulted in a 700% increase in flight velocity (from 30.6 m/s to 244.8 m/s) and a corresponding 284% rise in propulsive power (from 1.24 MW to 4.77 MW). However, this came at the cost of a 67% reduction in exhaust kinetic power (from 15.3 MW to 5.0 MW), which led to a net 10% decline in thermal efficiency.
- **Effect of Equivalence Ratio:** Increasing the equivalence ratio from 0.24 to 0.8 boosted net thrust by 68% (from 32.8 kN to 55.1 kN) and overall power by 61%, but also caused an 86% rise in SFC. Thermal efficiency dropped by 34% as the equivalence ratio increased from 0.24 to 0.73, declining from 42% to 27.8% due to disproportionate increases in fuel input relative to power output. NO emissions increased non-linearly, rising from 0.02 g/s at an equivalence ratio of 0.24 to over 0.21 g/s at 0.8. Additionally, the marginal gains in thrust per unit of additional fuel input diminished significantly, with thrust increasing by only 5% when the equivalence ratio rose from 0.7 to 0.8, compared to a 27% increase between 0.4 and 0.5.

- Influence of FPR and BPR: Variations in FPR and BPR significantly impacted net thrust, SFC, and thermal efficiency. At a BPR of 5, increasing the FPR from 1.2 to 1.8 raised net thrust by 35% (from 46.4 kN to 62.6 kN) and reduced SFC by 26%. Similarly, at an FPR of 1.5, increasing BPR from 3 to 7 boosted net thrust by 28% (from 48.2 kN to 61.6 kN) and cut SFC by 22%. Thermal efficiency improved modestly, rising from 0.37 to 0.39 within the FPR (1.2–1.8) and BPR (3–7) range. Higher FPR increased NO production due to elevated core combustion temperatures, while BPR had negligible impact on NO emissions.
- Weight and Power-to-Weight Considerations: Integrating the SOFC-GT system into commercial aviation was shown to pose weight challenges. Even with optimistic 2030 SOFC weight estimates, the power-to-weight ratio of the hybrid system remained substantially lower than that of the conventional turbofan engine.

The findings confirm that SOFC-GT hybrid systems hold promise for future sustainable aviation, offering pathways to reduce greenhouse gas and NO_x emissions while maintaining competitive thrust and efficiency. However, several areas warrant further research and development.

First, a more sophisticated combustion model is required to accurately capture the combustion characteristics of ammonia–hydrogen flames, ensuring stable operation and reduced emissions over a wide range of conditions. Such a model should incorporate detailed chemical kinetics and turbulence-chemistry interactions to ensure stable operation, minimise emissions and optimise performance across varying equivalence ratios, fuel compositions, and operating regimes.

Furthermore, the stability and reliability of SOFCs under prolonged operational conditions, particularly in aviation, must be considered. SOFC attenuation, which encompasses degradation mechanisms affecting performance over time, is a critical factor for ensuring consistent power output and operational stability. Although not included in the current study, modelling and analysing attenuation dynamics is essential. Future studies should explore the interplay between SOFC degradation and hybrid system behaviour, with an emphasis on developing mitigation strategies such as advanced material designs and optimised operating conditions.

Additionally, exploring alternative SOFC designs and materials can enhance the power density, durability, and fuel flexibility of the fuel cell stack. Advances in electrolyte composition, electrode microstructure, and stack geometry may enable operation at lower temperatures or under higher pressure ratios, improving thermal integration with the gas turbine and increasing the overall efficiency. Such innovations would also support broader adoption of alternative fuels, including ammonia and hydrogen, while alleviating weight and integration challenges.

Beyond the combustion and SOFC aspects, future work should consider off-design analyses, transient behaviour, and operational constraints, including start-up times, load-following capability, and maintenance requirements. Addressing these practical considerations, alongside optimising engine components and integration strategies, will advance the realisation of SOFC-GT systems as viable solutions for cleaner and more efficient aviation.

CRedit authorship contribution statement

Luca Wagner: Writing – original draft, Visualization, Validation, Software, Methodology, Investigation, Formal analysis, Data curation. **Efstathios-Al. Tingas:** Writing – review & editing, Supervision, Resources, Project administration, Methodology, Investigation, Funding acquisition, Conceptualization.

Declaration of Generative AI and AI-assisted technologies in the writing process

During the preparation of this work the authors used ChatGPT in order to improve the readability and language of the manuscript. After using this tool/service, the authors reviewed and edited the content as needed and take full responsibility for the content of the published article.

Declaration of competing interest

The authors declare the following financial interests/personal relationships which may be considered as potential competing interests: Luca Wagner reports financial support was provided by Edinburgh Napier University. If there are other authors, they declare that they have no known competing financial interests or personal relationships that could have appeared to influence the work reported in this paper.

Acknowledgements

This work was partly supported by Edinburgh Napier University, United Kingdom.

Appendix A. Supplementary data

Supplementary material related to this article can be found online at <https://doi.org/10.1016/j.enconman.2025.119861>.

Data availability

Data will be made available on request.

References

- [1] Commission E, for Research D-G, Innovation. Fly the green deal – Europe's vision for sustainable aviation. Publications Office of the European Union; 2022. <http://dx.doi.org/10.2777/732726>.
- [2] Air Transport Action Group. Waypoint 2050. 2021. https://aviationbenefits.org/media/167417/w2050_v2021_27sept_full.pdf. [Accessed 24 September 2023].
- [3] Administration FA. United States 2021 aviation climate action plan. 2024. URL <https://www.faa.gov/sustainability/aviation-climate-action-plan>. [Accessed 24 February 2024].
- [4] Guo F, Li C, Liu H, Cheng K, Qin J. Matching and performance analysis of a solid oxide fuel cell turbine-less hybrid electric propulsion system on aircraft. *Energy* 2023;263:125655. <http://dx.doi.org/10.1016/j.energy.2022.125655>, URL <https://www.sciencedirect.com/science/article/pii/S0360544222025415>.
- [5] Kazula S, de Graaf S, Enghardt L. Review of fuel cell technologies and evaluation of their potential and challenges for electrified propulsion systems in commercial aviation. *J Glob Power Propuls Soc* 2023;7:43–57.
- [6] Azizi MA, Brouwer J. Progress in solid oxide fuel cell-gas turbine hybrid power systems: System design and analysis, transient operation, controls and optimization. *Appl Energy* 2018;215:237–89.
- [7] Hedberg G, Hamilton R, McLarty D. Design and performance analysis of a de-coupled solid oxide fuel cell gas turbine hybrid. *Int J Hydrog Energy* 2020;45(55):30980–93.
- [8] Ji Z, Qin J, Cheng K, Guo F, Zhang S, Dong P. Thermodynamics analysis of a turbojet engine integrated with a fuel cell and steam injection for high-speed flight. *Energy* 2019;185:190–201.
- [9] Ji Z, Qin J, Cheng K, Liu H, Zhang S, Dong P. Thermodynamic analysis of a solid oxide fuel cell jet hybrid engine for long-endurance unmanned air vehicles. *Energy Convers Manage* 2019;183:50–64.
- [10] Ji Z, Qin J, Cheng K, Guo F, Zhang S, Zhou C, Dong P. Determination of the safe operation zone for a turbine-less and solid oxide fuel cell hybrid electric jet engine on unmanned aerial vehicles. *Energy* 2020;202:117532.
- [11] Ji Z, Rokni MM, Qin J, Zhang S, Dong P. Performance and size optimization of the turbine-less engine integrated solid oxide fuel cells on unmanned aerial vehicles with long endurance. *Appl Energy* 2021;299:117301.
- [12] Guo F, Li C, Liu H, Cheng K, Qin J. Matching and performance analysis of a solid oxide fuel cell turbine-less hybrid electric propulsion system on aircraft. *Energy* 2023;263:125655.
- [13] Ji Z, Qin J, Cheng K, Guo F, Zhang S, Dong P. Performance characteristics of a solid oxide fuel cell hybrid jet engine under different operating modes. *Aerospace Technol* 2020;105:106027.

- [14] Seyam S, Dincer I, Agelin-Chaab M. Investigation of two hybrid aircraft propulsion and powering systems using alternative fuels. *Energy* 2021;232:121037.
- [15] Ji Z, Qin J, Cheng K, Guo F, Zhang S, Dong P. Comparative performance analysis of solid oxide fuel cell turbine-less jet engines for electric propulsion airplanes: Application of alternative fuel. *Aerosp Sci Technol* 2019;93:105286.
- [16] Seyam S, Dincer I, Agelin-Chaab M. Environmental impact assessment of a newly developed solid oxide fuel cell-based system combined with propulsion engine using various fuel blends for cleaner operations. *Sustain Mater Technol* 2023;35:e00554.
- [17] Liu H, Qin J, Xiu X, Ha C, Dong P. Comparative study of fuel types on solid oxide fuel cell-gas turbine hybrid system for electric propulsion aircraft. *Fuel* 2023;347:128426.
- [18] Seyam S, Dincer I, Agelin-Chaab M. Novel hybrid aircraft propulsion systems using hydrogen, methane, methanol, ethanol and dimethyl ether as alternative fuels. *Energy Convers Manage* 2021;238:114172.
- [19] Ji Z, Qin J, Cheng K, Liu H, Zhang S, Dong P. Performance evaluation of a turbojet engine integrated with interstage turbine burner and solid oxide fuel cell. *Energy* 2019;168:702–11.
- [20] Liu H, Qin J, Ji Z, Guo F, Dong P. Study on the performance comparison of three configurations of aviation fuel cell gas turbine hybrid power generation system. *J Power Sources* 2021;501:230007.
- [21] Rupiper LN, Skabelund BB, Ghotkar R, Milcarek RJ. Impact of fuel type on the performance of a solid oxide fuel cell integrated with a gas turbine. *Sustain Energy Technol Assess* 2022;51:101959.
- [22] Mejías RB, Saias CA, Roumeliotis I, Pachidis V, Bacic M. Assessment of hydrogen gas turbine-fuel cell powerplant for rotorcraft. *Int J Hydrog Energy* 2024;50:772–83.
- [23] Guo F, Li C, Xiu X, Cheng K, Qin J. Comprehensive technical analyses of a solid oxide fuel cell turbine-less hybrid aircraft propulsion system using ammonia and methane as alternative fuels. *Appl Therm Eng* 2023;230:120787.
- [24] Otto M, Vesely L, Kapat J, Stoia M, Applegate ND, Natsui G. Ammonia as an aircraft fuel: A critical assessment from airport to wake. *ASME Open J Eng* 2023;2.
- [25] Valera-Medina A, Morris S, Runyon J, Pugh DG, Marsh R, Beasley P, Hughes T. Ammonia, methane and hydrogen for gas turbines. *Energy Procedia* 2015;75:118–23.
- [26] Paterson G, Tingas E-A, Hardalupas Y, Taylor AM. Engine performance and emissions from a fumigated hydrogen/ammonia compression ignition engine with a hydrogen peroxide pilot. *Int J Hydrog Energy* 2024;67:334–50.
- [27] Kumar L, Sleiti AK. Systematic review on ammonia as a sustainable fuel for combustion. *Renew Sustain Energy Rev* 2024;202:114699.
- [28] Aziz M, Juangsa FB, Irhamna AR, Irsyad AR, Hariana H, Darmawan A. Ammonia utilization technology for thermal power generation: A review. *J Energy Inst* 2023;111:101365.
- [29] Berwal P, Kumar S, Khandelwal B. A comprehensive review on synthesis, chemical kinetics, and practical application of ammonia as future fuel for combustion. *J Energy Inst* 2021;99:273–98.
- [30] El-Adawy M, Nemitallah MA, Abdelhafez A. Towards sustainable hydrogen and ammonia internal combustion engines: Challenges and opportunities. *Fuel* 2024;364:131090.
- [31] Klawitter M, Wüthrich S, Cartier P, Albrecht P, Herrmann K, Gößnitzer C, Pirker G, Wimmer A. Ammonia as a fuel: Optical investigation of turbulent flame propagation of NH₃/air and NH₃/H₂/N₂/Air flames at engine conditions. *Fuel* 2024;375:132616.
- [32] Aalrebei OF, Al Assaf AH, Amhamed A, Swaminathan N, Hewlett S. Ammonia-hydrogen-air gas turbine cycle and control analyses. *Int J Hydrog Energy* 2022;47(13):8603–20.
- [33] Chapman JW, Lavelle TM, May RD, Litt JS, Guo T-H. Toolbox for the modeling and analysis of thermodynamic systems (T-MATS) user's guide, NASA/TM—2014–216638. Tech. rep., 2014.
- [34] Chapman JW, Lavelle TM, May R, Litt JS, Guo T-H. Propulsion system simulation using the toolbox for the modeling and analysis of thermodynamic systems (t-mats). In: 50th AIAA/aSME/SAE/ASEE joint propulsion conference. 2014, p. 3929.
- [35] Chapman JW, Lavelle TM, Litt JS, Guo T-H. A process for the creation of T-MATS propulsion system models from npss data. In: 50th AIAA/aSME/SAE/ASEE joint propulsion conference. 2014, p. 3931.
- [36] Zinnecker A, Chapman JW, Lavelle TM, Litt JS. Development of a twin-spool turbofan engine simulation using the toolbox for modeling and analysis of thermodynamic systems (t-mats). In: 50th AIAA/aSME/SAE/ASEE joint propulsion conference. 2014, p. 3930.
- [37] Lavelle TM, Chapman JW, May RD, Litt JS, Guo T-H. Cantera integration with the toolbox for modeling and analysis of thermodynamic systems (t-mats). In: AIAA/aSME/SAE/ASEE joint propulsion conference. 2014, no. GRC-E-DAA-TN16145.
- [38] Kalinci Y, Dincer I. Analysis and performance assessment of NH₃ and H₂ fed SOFC with proton-conducting electrolyte. *Int J Hydrog Energy* 2018;43(11):5795–807. <http://dx.doi.org/10.1016/j.ijhydene.2017.07.234>, URL <https://www.sciencedirect.com/science/article/pii/S0360319917331488>.
- [39] Guo F, Qin J, Ji Z, Liu H, Cheng K, Zhang S. Performance analysis of a turbofan engine integrated with solid oxide fuel cells based on Al-H₂O hydrogen production for more electric long-endurance UAVs. *Energy Convers Manage* 2021;235:113999.
- [40] Ji Z, Qin J, Cheng K, Dang C, Zhang S, Dong P. Thermodynamic performance evaluation of a turbine-less jet engine integrated with solid oxide fuel cells for unmanned aerial vehicles. *Appl Therm Eng* 2019;160:114093.
- [41] Zhao F, Virkar AV. Dependence of polarization in anode-supported solid oxide fuel cells on various cell parameters. *J Power Sources* 2005;141(1):79–95. <http://dx.doi.org/10.1016/j.jpowsour.2004.08.057>, URL <https://www.sciencedirect.com/science/article/pii/S0378775304009528>.
- [42] Zhang M, An Z, Wang L, Wei X, Jianayihan B, Wang J, Huang Z, Tan H. The regulation effect of methane and hydrogen on the emission characteristics of ammonia/air combustion in a model combustor. *Int J Hydrog Energy* 2021;46(40):21013–25.
- [43] Ji Z, Qin J, Cheng K, Liu H, Zhang S, Dong P. Design and performance of a compact air-breathing jet hybrid-electric engine coupled with solid oxide fuel cells. *Front Energy Res* 2021;8:613205.
- [44] Valencia EA, Hidalgo V, Panagiotis L, Nalianda D, Singh R, Liu C. Design point analysis of an hybrid fuel cell gas turbine cycle for advanced distributed propulsion systems. In: 51st AIAA/SAE/ASEE joint propulsion conference. 2015, p. 3802.
- [45] Guynn MD, Freh JE, Olson ED. Evaluation of a hydrogen fuel cell powered blended-wing-body aircraft concept for reduced noise and emissions, NASA/TM-2004–212989. Tech. rep., 2004.